The Astrophysical Journal, 812:155 (22pp), 2015 October 20 doi:10.1088/0004-637X/812/2/155
© 2015. The American Astronomical Society. All rights reserved.

SHARDS: A GLOBAL VIEW OF THE STAR FORMATION ACTIVITY AT $z \sim 0.84$ and $z \sim 1.23$

Antonio Cava[1], Pablo G. Pérez-González[2], M. Carmen Eliche-Moral[2], Elena Ricciardelli[3], Alba Vidal-García[4], Belen Alcalde Pampliega[2], Almudena Alonso-Herrero[5], Guillermo Barro[6], Nicolas Cardiel[2], A. Javier Cenarro[7], Stephane Charlot[4], Emanuele Daddi[8], Miroslava Dessauges-Zavadsky[1], Helena Domínguez Sánchez[2], Nestor Espino-Briones[2], Pilar Esquej[2], Jesus Gallego[2], Antonio Hernán-Caballero[5], Marc Huertas-Company[9], Anton M. Koekemoer[10], Casiana Muñoz-Tunon[11], Jose M. Rodriguez-Espinosa[11], Lucia Rodríguez-Muñoz[2,12], Laurence Tresse[13], and Victor Villar[14]

[1] Observatoire de Genève, Université de Genève, 51 Ch. des Maillettes, 1290 Versoix, Switzerland
[2] Departamento de Astrofísica y Ciencias de la Atmósfera, Facultad de CC. Físicas, Universidad Complutense de Madrid, E-28040, Madrid, Spain
[3] Departament d'Astronomia i Astrofisica, Universitat de Valencia, c/Dr. Moliner 50, E-46100 Burjassot, Valencia, Spain
[4] Institut d'Astrophysique de Paris, CNRS, Université Pierre & Marie Curie, UMR 7095, 98bis bd Arago, F-75014 Paris, France
[5] Instituto de Física de Cantabria, CSIC-UC, Avenida de los Castros s/n, E-39005 Santander, Spain
[6] UCO/Lick Observatory, Department of Astronomy and Astrophysics, University of California, Santa Cruz, CA 95064, USA
[7] Centro de Estudios de Física del Cosmos de Aragón (CEFCA), Plaza San Juan 1, E-44001 Teruel, Spain
[8] CEA, Laboratoire AIM, Irfu/SAp, F-91191 Gif-sur-Yvette, France
[9] University Denis Diderot, CNRS, GEPI-Observatoire de Paris UMR 8111, Paris, France
[10] Space Telescope Science Institute, 3700 San Martin Dr., Baltimore, MD 21218, USA
[11] Instituto de Astrofísica de Canarias, 38200 La Laguna, Tenerife; Departamento de Astrofísica, Universidad de La Laguna, E-38205 La Laguna, Tenerife, Spain
[12] Dipartimento di Fisica e Astronomia "G. Galilei", Universitá di Padova, Vicolo dell'Osservatorio 3, I-35122, Italy
[13] Aix Marseille Université, CNRS, LAM (Laboratoire d'Astrophysique de Marseille) UMR 7326, F-13388, Marseille, France
[14] European Space Astronomy Centre, P.O. Box 78, E-28691 Villanueva de la Canada, Madrid, Spain
Received 2015 July 22; accepted 2015 September 8; published 2015 October 20

ABSTRACT

In this paper, we present a comprehensive analysis of star-forming galaxies (SFGs) at intermediate redshifts ($z \sim 1$). We combine the ultra-deep optical spectro-photometric data from the Survey for High-z Absorption Red and Dead Sources (SHARDS) with deep UV-to-FIR observations in the GOODS-N field. Exploiting two of the 25 SHARDS medium-band filters, F687W17 and F823W17, we select [O II] emission line galaxies at $z \sim 0.84$ and $z \sim 1.23$ and characterize their physical properties. Their rest-frame equivalent widths (EW_{rf}([O II])), line fluxes, luminosities, star formation rates (SFRs), and dust attenuation properties are investigated. The evolution of EW_{rf}([O II]) closely follows the SFR density evolution of the universe, with a trend of $EW_{rf}([O\,II]) \propto (1+z)^3$ up to redshift $z \simeq 1$, followed by a possible flattening. The SF properties of the galaxies selected on the basis of their [O II] emission are compared with complementary samples of SFGs selected by their MIR and FIR emission, and also with a general mass-selected sample of galaxies at the same redshifts. We demonstrate observationally that the *UVJ* diagram (or, similarly, a cut in the specific SFR) is only partially able to distinguish the quiescent galaxies from the SFGs. The SFR–M_* relation is investigated for the different samples, yielding a logarithmic slope $\sim$1, in good agreement with previous results. The dust attenuations derived from different SFR indicators (UV(1600), UV (2800), [O II], IR) are compared and show clear trends with respect to both the stellar mass and total SFR, with more massive and highly star-forming galaxies being affected by stronger dust attenuation.

Key words: galaxies: evolution – galaxies: general – galaxies: high-redshift – galaxies: photometry – galaxies: star formation – quasars: emission lines

1. INTRODUCTION

The study of emission line galaxies (ELGs) has long been recognized as one of the most powerful and direct tools to investigate star-forming galaxies (SFGs) at different redshifts. For local SFGs, the most common and reliable emission line used to investigate star formation (SF) is Hα (see, e.g., Gallego et al. 1995; Tresse & Maddox 1998; Pérez-González et al. 2003; Domínguez Sánchez et al. 2012). At increasing redshifts other lines and methods must be used because the Hα line runs out of the optical and near-infrared (NIR) range, becoming more difficult to observe. Present-day NIR facilities allow these local studies to be extended to higher redshifts using spectroscopy (see, e.g., Tresse et al. 2002; Twite et al. 2012) or narrow-band photometry (see, e.g., Villar et al. 2008, 2011; Sobral et al. 2009b, 2011, 2013; Ly et al. 2011), although it remains difficult and expensive, in terms of observing time, to obtain deep and wide surveys of line emitters with these instruments.

One of the most popular SF indicators used at intermediate/high redshift is the [O II] emission line at 3727 Å. This line lies at optical wavelengths up to $z \sim 1.5$, so it has been widely used to detect and study SFGs for decades. The physical mechanism responsible for the production of this intense emission line (actually a doublet at 3726 and 3729 Å) has been investigated and well understood for a long time (Eddington 1927), but the relation between environmental conditions (density, temperature, metallicity, ionization state of the gas, ...) and the intrinsic emitted flux is still far from being completely characterized. Nonetheless, [O II] has proved to be a very useful indicator of star formation rate (SFR), and empirical calibrations are commonly used to transform [O II] luminosities into SFR (Gallagher et al. 1989; Hogg et al. 1998; Kennicutt 1998; Jansen et al. 2001; Kewley et al. 2004; Moustakas & Kennicutt 2006; Yan et al. 2006; Garn & Best 2010; Gilbank et al. 2010, 2011; Hayashi et al. 2013).

The Survey for High-z Absorption Red and Dead Sources (SHARDS[15], Pérez-González et al. 2013) is an ESO/GTC Large Program carried out with the OSIRIS instrument on the 10.4 m Gran Telescopio Canarias (GTC). Our survey has obtained imaging data in the GOODS-N field through 25 medium-band filters covering the wavelength range between 500 and 950 nm in subarcsec seeing conditions. The typical width of our filters is 15 nm for wavelengths bluer than 880 nm, and 25–35 nm for the three reddest filters. In each filter, SHARDS is able to detect 26.5 mag sources at the 3σ level (at least). SHARDS allows us to study any isolated emission line falling within its wavelength coverage. More specifically, for the [O II] line, we can cover the interval from $z \sim 0.3$ up to $z \sim 1.6$. In this work, we focus on the analysis of ELGs selected using two of the 25 SHARDS filters, the F687W17 and F823W17, corresponding to ELGs at $z \simeq 0.84$ and $z \simeq 1.23$ respectively. We have chosen these two filters because they are representative enough of the whole data set and they provide two samples of galaxies that are sufficiently separated in redshift ($\sim$1.5 Gyr in time) to allow an investigation of the possible evolutionary effects on the derived physical properties. A more extensive analysis including all the SHARDS filters will be presented in a future work.

One of the aims of this work is to demonstrate the power of the SHARDS medium-band data to select ELGs down to very faint continuum magnitudes and line fluxes (similar to or even fainter that those characteristic of the deepest spectroscopic and narrow-band surveys) and study their physical properties in detail. Even though the equivalent spectral resolution of SHARDS ($R \sim 50$) is smaller than that reached by typical spectroscopic (e.g., TKRS, VVDS, DEEP3, HETDEX, or MOSDEF surveys; Wirth et al. 2004; Le Fèvre et al. 2005; Adams et al. 2011; Cooper et al. 2011; Kriek et al. 2015) or narrow-band surveys (Villar et al. 2008, 2011; Sobral et al. 2009b, 2010, 2011, 2012, 2013), the depth and quality of the SHARDS data compensate for this a priori disadvantage, allowing us to study stellar mass-complete samples down to $M_* \sim 10^9\ M_\odot$ at $z \sim 1$ (Hernán-Caballero et al. 2014).

In fact, our medium-band survey can reach deeper magnitudes (down to $R \sim 26$–27) than a typical spectroscopic survey (limited to $R \sim 24$–25) by investing a substantially smaller amount of observing time and overcoming the issues arising when dealing with slit apertures and the limited multiplexing of spectrographs. On the other hand, integral field unit (IFU) spectrographs can also observe all the sources within their field of view (FOV), but this is normally very limited, while the SHARDS filters apply to the relatively wide OSIRIS@GTC FOV (i.e., $\sim 7' \times 8'$). Furthermore, ultra-deep medium-band selected SF galaxy samples should be less affected by Malmquist bias than spectroscopically observed samples, which tend to favor highly star-forming galaxies. We also remark that systematic effects are expected to be introduced in the study of emission-line luminosity functions by the typical selection of targets in spectroscopic surveys, which are typically based on magnitude cuts (i.e., continuum-dominated) and may miss faint galaxies with strong emission lines (i.e., large equivalent widths (EWs)). These biases can also affect the study of the SFR–M_* relation since at low masses the success rate of getting redshifts may be higher if the SFR is above average whereas it may be lower for massive, heavily attenuated galaxies (see, e.g., Rodighiero et al. 2014; Speagle et al. 2014, for a discussion of the biases and selection effects on the SFR–M_* relation), thus introducing a flattening in the SFR–M_* relation. Medium- and narrow-band surveys are, by nature, less prone to this kind of selection bias.

The so-called "main sequence" (Noeske et al. 2007) of SF galaxies has been extensively studied in the past using different sample selections from low redshift (see, e.g., Brinchmann et al. 2004; Elbaz et al. 2007; Ilbert et al. 2015) to high redshift (see, e.g., Speagle et al. 2014; Steinhardt et al. 2014; Salmon et al. 2015; Schreiber et al. 2015) in different environments, ranging from extremely low density (known as cosmic voids; see Ricciardelli et al. 2014) to the most crowded regions of the universe (i.e., filaments and galaxy clusters; see e.g., Vulcani et al. 2010, 2015; Koyama et al. 2013; Darvish et al. 2014), and using various diagnostics as SFR indicators (see, e.g., Rodighiero et al. 2014; Shivaei et al. 2015a, 2015b). Despite the advancements in this topic, the debate on the nature and characteristics of the galaxies populating the main sequence is still open (see, e.g., Kelson 2014 for a different interpretation of the star-forming main sequence). As indicated above, the determination of the slope and the scatter of this relation and the comparison between different works is made difficult by various systematic effects (e.g., differences in calibrations, selection biases, SFR indicator used, among others; see Speagle et al. 2014 for a more complete discussion of these uncertainties). Furthermore, to disentangle the differences in the determination of the main sequence due to the mentioned systematic effects from those due to purely evolutionary effects can be even more subtle.

The main aims of this paper are: (1) to exploit the ultra-deep SHARDS data to select and investigate intermediate-redshift ELGs on the basis of their [O II] emission and (2) to perform an (almost) unbiased study of the SF activity of galaxies at intermediate redshifts ($\sim$1). This goal is attained by combining ultra-deep medium-band and multi-wavelength data (from UV to FIR) and comparing various SF indicators (UV, [O II] IR) to assess the robustness of the results. In particular we focus on (3) the characterization of the SFR–M_* relation and (4) the dependence of the dust attenuation on the physical galaxy properties (M_* and total SFR). The depth and quality of SHARDS data allow us to improve upon previous intermediate-redshift studies going down to fainter magnitudes and limiting the effect of the selection biases typical of spectroscopic surveys.

The scheme of this paper follows. In Section 2, we summarize the main characteristics of the survey and the data used in this work. We introduce the sample selection for [O II] galaxies and we define the different complementary samples (general stellar mass-selected sample, IR-detected and UVJ/quiescent galaxies) used throughout the paper. We present the methods used to select ELGs, their redshift distribution and discuss the adopted procedures and caveats. In Section 3, we present the basic measurements for the EWs and line fluxes characterizing the [O II] population and discuss their observational properties. In Section 4, we discuss the [O II]-based SFRs (SFR([O II])), the stellar mass–SFR relation, and their stellar population properties (mass and age distributions). In Section 5, we compare the properties for different sample selections and discuss the derived SFR–M_* relations and the differences

[15] The SHARDS web page is available at: http://guaix.fis.ucm.es/~pgperez/SHARDS/.

induced by each selection. Dust extinction and its dependence on the stellar mass and the SFR are investigated in Section 6. Main results and conclusions are summarized in Section 7.

Throughout this paper we use AB magnitudes and the Chabrier (2003) initial mass function (IMF). We adopt the cosmology $H_0 = 70$ km s^{-1} Mpc^{-1}, $\Omega_m = 0.3$, and $\Omega_\lambda = 0.7$.

2. DATA AND SAMPLE SELECTION

In this work, we have gathered a complete sample of star-forming galaxies at $z \sim 0.84$ and $z \sim 1.23$ in the GOODS-N field by combining three different selections: a pure stellar mass-selected sample of galaxies with SFRs calculated through the rest-frame UV emission at 150–250 nm, an emission-line selection based on the detection of the [O II]λ3727 line with data from the SHARDS (Pérez-González et al. 2013), and a selection of obscured SFGs based on mid- and far-IR data from *Spitzer* and *Herschel*. In the following subsections, we present the details about the different data sets used in the selection of SFGs and their characterization. We start with the description of the most notable selection among the three mentioned above: the [O II] sample selected with the new SHARDS data (see Sections 2.1–2.3). Then, we complement this sample with the other selections and perform a comparison of the properties of the sample of [O II] emitters with the dust-obscured SFGs selected from IR data and the mass-selected sample (characterized by the UV emission, see Sections 2.4–2.5). This approach gives us a comprehensive view of the typical limitations inherent in the different selection methods and highlights the complementarity of the different selected samples. As we will discuss later, the construction of the complementary samples must take into account the fact that the [O II] emitters selected with SHARDS have a very specific redshift distribution. Therefore, both the mass-selected and the obscured SFG samples should follow similar redshift distributions. This is mandatory to be able to make a fair comparison between different samples and understand the SF and dust extincion properties of the whole population of SFGs at $z \sim 0.84$ and $z \sim 1.23$, which we will discuss in Sections 4–6.

2.1. Data Sets Gathered for this Work

GOODS-N is one of the most targeted areas of the sky at all wavelengths. For this work, apart from our new SHARDS data, we have combined the wealth of deep and high-quality ancillary data, ranging from an ultra-deep X-ray exposure (2 Ms Chandra Deep Field North (CDFN), Alexander et al. 2003) to the deepest data in the MIR/FIR with surveys such as GOODS (Giavalisco et al. 2004), FIDEL (Frayer et al. 2006), PEP (Lutz et al. 2011), HerMES (Oliver et al. 2010), and *Herschel*-GOODS (Elbaz et al. 2011). Multiple spectroscopic redshifts for faint targets are also available (Cowie et al. 2004; Wirth et al. 2004; Reddy et al. 2005, 2006; Barger et al. 2008; Cooper et al. 2011; Kriek et al. 2015).

The SHARDS project was designed to be able to measure absorption indices such as Mg_{UV} or D4000 for galaxies at $z = 1.0$–2.5 through imaging data, and detect ELGs up to $z \sim 7$. For those purposes, SHARDS obtained imaging data in the GOODS-N field through 25 medium-band filters covering the wavelength range between 500 and 950 nm in subarcsec seeing conditions. The typical width of our filters is 15 nm for wavelengths bluer than 880 nm, and 25–35 nm for the three reddest filters. In each filter, SHARDS is able to detect 26.5 mag sources at the 3σ level (at least). Virtually all of the deep region covered by GOODS with *Hubble Space Telescope* (*HST*)/Advanced Camera for Surveys (ACS) is surveyed by SHARDS using two GTC/OSIRIS pointings, adding up to a total surveyed area of $\sim$130 arcmin^2 (see Figure 2 from Pérez-González et al. 2013). The observations carried out by SHARDS allow us to accurately determine the main properties of the stellar populations present in these galaxies through spectro-photometric data with a resolution $R \sim 50$, sufficient to measure absorption indices such as the D4000 index (e.g., Bruzual 1983; Balogh et al. 1999; Kauffmann et al. 2003; Kriek et al. 2011; Hernán-Caballero et al. 2013, 2014) or Mg_{UV} index (Spinrad et al. 1997; McCarthy et al. 2004; Daddi et al. 2005; Saracco et al. 2005; Cimatti et al. 2008; Pérez-González et al. 2013). At this spectral resolution, it is also possible to detect emission lines and measure their fluxes and EWs. SHARDS can detect the lines Hα, [O II], [O III], Lyα, among others (see, e.g., Villar et al. 2011; Pérez-González et al. 2013; Sobral et al. 2013).

As explained in Pérez-González et al. (2013), given the special characteristics of the OSIRIS instrument at GTC, within each single frame taken with a given physical filter, each pixel sees a different passband. To overcome this issue, we performed a detailed calibration as a function of the position in the FOV. The significant variation of the passband seen by each point of the detector is a function of the position in the FOV and implies a complex behavior of the absolute photometric calibration of the SHARDS images. To cope with these issues, we developed a special flux calibration procedure, aimed at determining the zeropoint of the SHARDS mosaics in each filter as a function of position in the image. The flux calibration of the SHARDS mosaics was performed by comparing the measured photometry in our images with spectroscopic data for several sources in the field.

To complement the SHARDS data, we also benefitted from the fact that GOODS-N has been observed by *HST* with ACS and WFC3 providing slitless, intermediate-resolution spectroscopy in the optical (through the G800L grism; PEARS, Kümmel et al. 2009; see also Pirzkal et al. 2004, 2009) and NIR (G102; PI: G. Barro, G141; PI: B. Weiner). In addition, the availability of the deepest IRAC ([3.6 μm] < 26.0 mag) and MIPS ($F_{5\sigma}$[24 μm] > 30 μJy) observations ensures the detection of the rest-frame NIR/MIR emission of the galaxies and allow us to estimate robust stellar masses and SFRs (Pérez-González et al. 2005, 2008; Cimatti et al. 2008).

We merged all these data set for a mass-selected sample as described in Pérez-González et al. (2008). In that paper, we built spectral energy distributions (SEDs) using aperture photometry and deconvolution algorithms for IRAC bands. We then fitted the SEDs with a set of templates representative of the diverse galaxy populations and built with stellar population synthesis models. These fits allowed us to obtain estimations of the photometric redshifts and stellar masses. We describe this modeling in more detail in Sections 2.2 and 3. Based on the models best fitting the photometric data, we also obtained luminosities in the rest-frame UV (more specifically, at 150 and 280 nm), which were then converted to SFRs using the recipes from Barro et al. (2011b), taken from Bell et al. (2005). Attenuations based on the UV slope β were also estimated using the attenuation law of Calzetti et al. (2000) and the SFR(IR)/SFR(UV) versus β calibration in Meurer et al.

(1999). We will discuss the UV-based SFRs in detail in Section 5.

2.2. Photometry and SED Fitting

In this section, we briefly summarize the basic steps and procedures adopted to extract the photometry and to fit the SEDs of different galaxy samples. These steps are performed exploiting the Rainbow Cosmological Surveys Database[16] hosted by the Universidad Complutense of Madrid, which is the central repository for all the SHARDS and ancillary data used in this paper.

Photometry is performed using the Rainbow (G. Barro et al. 2015, in preparation) tools that are able to carry out simultaneous photometry in multiple bands using prior-based positions and apertures. The priors for the SHARDS extraction are based on SExtractor (Bertin & Arnouts 1996) catalogs and Kron (1980) apertures obtained as an average of those measured in all SHARDS bands. Photometry for longer wavelength bands (starting with IRAC) is extracted using circular apertures of fixed sizes.

For the SED fitting procedure, we adopt a two-population model, each population described by a SF history (SFH) following an exponentially declining law, characterized by timescales $\tau_{\rm you}$ and a $\tau_{\rm old}$ parameter for the young and the old stellar populations, respectively. We use the models from Bruzual & Charlot (2003), with a Chabrier (2003) IMF spanning stellar masses from 0.1 to 100 $M_{\odot}$. We assume the dust attenuation law from Calzetti et al. (2000). For the whole sample of [O II] emitter candidates selected from SHARDS and the complementary samples described in Sections 2.3 and 2.4 we derive stellar masses, SFRs, dust reddening $A(V)$, and stellar ages from the best fits.

We compare the photometric data with a grid of models probing τ values in the range $6 \leqslant \log(\tau/{\rm yr}) \leqslant 12$ for each population. These τ values were selected to include SFHs from instantaneous to roughly constant. The grid of models spans a range of ages, from 1 Myr to up to 1 Gyr for the young population and from 1 Gyr up to the age of the universe at the given galaxy redshift for the old population. We adopt a Calzetti et al. (2000) dust attenuation law and dust extinctions with $A_{\rm you}(V) = 0.0$–7.0 mag and $A_{\rm old}(V) = 0.0$–2.0 mag, with 0.1 mag increments. We consider the six metallicities available from the libraries of Bruzual & Charlot (2003). Additional details and an example of the stellar population fits in the SHARDS spectral region are given in Section 3.1. In these fits, the redshifts are fixed to either the spectroscopic values when available or the best photometric redshift solution. As we show in Section 2.3.2, we have a considerable improvement on the photometric redshift determination using the full SHARDS data set to perform SED fitting (G. Barro et al. 2015, in preparation; see also Ferreras et al. 2014).

We remark that the results obtained from this modeling are of particular relevance for the determination of the continuum at the wavelength of the [O II] emission line, as discussed in Section 3.

[16] The Rainbow Cosmological Surveys database is a vast compilation of photometric and spectroscopic data for several of the deepest cosmological fields, such as GOODS-north and -south, COSMOS, or the Extended Groth Strip, among others. It is publicly accessible through the website: https://rainbowx.fis.ucm.es/.

2.3. Sample Selection of [O II] Emitters

We have developed a novel selection technique to identify ELGs using the SHARDS medium-band spectro-photometric data set, based on similar narrow-band selection techniques. The technique to select SFGs (and also active galactic nuclei (AGNs)) from medium-band photometry is based on comparing the flux measured in one filter (the *central filter*, hereafter) with the fluxes obtained in two adjacent filters (the *continuum filters*, hereafter). Galaxies presenting emission lines would then pop-up in the central filter if their redshifts move the line within the passband of this filter, thus providing the emission line flux, while the adjacent filters would give us an estimate of the continuum around the emission line.

A similar color-excess technique has been applied to multiple surveys of intermediate, high, and very high redshifts (focusing on different lines such as Hα or Lyα) using typically narrow-band passbands as the central filter and a broad-band passband as the continuum filter (see, e.g., Ouchi et al. 2008; Villar et al. 2008, 2011; Sobral et al. 2009a, 2009b, 2012, 2013; Matthee et al. 2014).

Note that our data set consists of medium-band filters, not narrow-band, with a typical equivalent spectral resolution $R \sim 50$ to be compared, e.g., to $R \sim 100$ in Villar et al. (2008, 2011) or $R \sim 80$ in Sobral et al. (2009b, 2012, 2013), but the depth and image quality of the SHARDS images, jointly with the use of adjacent medium-band passbands for the determination of the continuum, offer several advantages over previous surveys as detailed next. Note also that the SHARDS spectral resolution is similar to that achieved with *HST* optical grism spectroscopy.

2.3.1. Selection of ELG Candidates Using SHARDS Data

In this work, we used two SHARDS filters as central passbands, F687W17 and F823W17, two of the deepest in our survey, centered at 687 and 823 nm, respectively. The most common emission line detected with these filters is [O II] λ3727, which means that the central wavelength corresponds approximately to a redshift of $z \sim 0.84$ or $z \sim 1.23$ for the bulk of our emission-line galaxy sample. We start the analysis of SHARDS-selected ELGs with these two filters because (1) they are representative enough of the whole data set, (2) they are two of the deepest ones, and (3) they enable the study of samples of galaxies located at sufficiently separated redshifts in order to unveil the possible evolutionary effects on their derived physical properties. In a future work we will present more extensive results including all the SHARDS filters.

In order to be able to compute the continuum level, we have also used data in four additional filters (lying on the bluer and redder sides of each central filter), namely F670W17, F704W17, F806W17, and F840W17. The main characteristics of the central and continuum filters and observed data used in this work are summarized in Table 1.

A sketch of the technique used in the selection of the ELGs sample is presented in Figure 1. We compare the magnitude in the central filter (F687W17 or F823W17) with that in the continuum filters (a combination of the two adjacent ones for each central filter). Typically, the estimation of the continuum in ELGs is carried out with broad-band filters, and also includes the line entering the central filter and possibly others (Villar et al. 2008, 2011; Sobral et al. 2009b, 2012, 2013). By using two adjacent medium-band filters, we can estimate a more accurate continuum level. This method can be considered robust for the

Table 1
Characteristics of the SHARDS Filters and Observations Used in this Study

Filter	CWL	Width	Exposure Time		$m_{3\sigma}$		Seeing	
			P1	P2	P1	P2	P1	P2
(1)	(2)	(3)	(4)	(4)	(5)	(5)	(6)	(6)
F670W17	670.4	16.0	3795	4554	26.8	26.9	0.8	1.0
F687W17	686.9	17.2	9270	12360	27.2	27.1	0.8	0.9
F704W17	703.7	17.9	6120	6120	26.8	26.8	0.9	0.9
F806W17	806.5	16.1	14900	14900	26.5	26.6	0.9	1.0
F823W17	823.1	14.7	18570	24760	26.8	26.8	0.8	0.9
F840W17	840.0	15.6	19530	25872	26.2	26.4	0.9	0.9

Note. (1) Filter name. (2) Central wavelength (in nm) of the filter for angle of incidence AOI = 10.°5 (approximately that for the center of the FOV). (3) Filter width (in nm). (4) Exposure time (in seconds). (5) Average 3σ depths (AB mag) for circular apertures of radius 0.″8 for pointings 1 and 2. (6) Average seeing (in arcsec) for pointings 1 and 2.

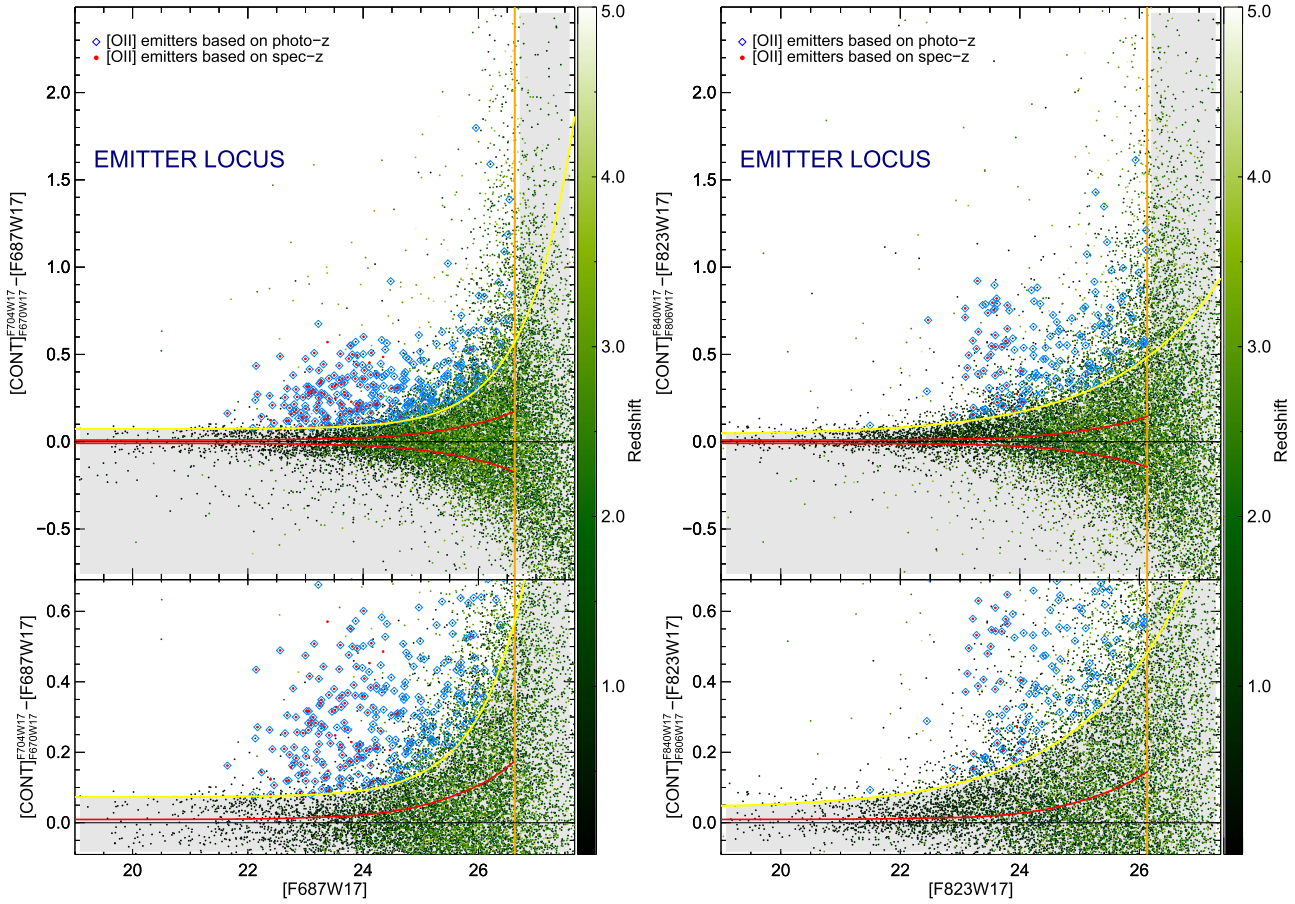

Figure 1. Color–magnitude diagram showing ELG candidates at ∼687 nm (left panel) and ∼823 nm (right panel). The vertical axis shows the color between a central SHARDS filter band and the average magnitude in the adjacent (continuum) SHARDS bands. The locus for galaxies with an emission line within the filter width detected with more than 2.5σ confidence is the region above the yellow-dashed curve, identified as the *emitter locus*. The vertical shaded orange line shows the minimum 3σ detection threshold of the SHARDS survey in the selected filter bands. Red dots indicate [O II] emitter candidates with spectroscopic confirmation, while blue diamonds stand for candidates selected using photometric redshifts. The red-dashed lines depict the typical photometric uncertainty as a function of the filter magnitude. Lower panels show an enlarged view around the selection curve.

continuum determination as long as the contribution of the emission line to the side filters can be neglected, which is typically the case for SHARDS filters (given the filter shape). Indeed, the SHARDS continuum coverage of the optical spectral range ensures that intrinsic variations of the spectral slope do not affect the continuum determination. The probability of another line entering the continuum filter is also smaller than when using broad-band filters. Nonetheless, the finite width of the filters, the noise, and other spectral features possibly falling in our observed spectral range can affect the final measurement. We rely on the interpolation between the two filters to define the observed continuum for the selection of ELGs. However, once the emission line candidates are selected, we perform a detailed SED fitting to fine-tune the continuum determination in order to obtain robust line fluxes and EWs (as described in Sections 2.2 and 3.1).

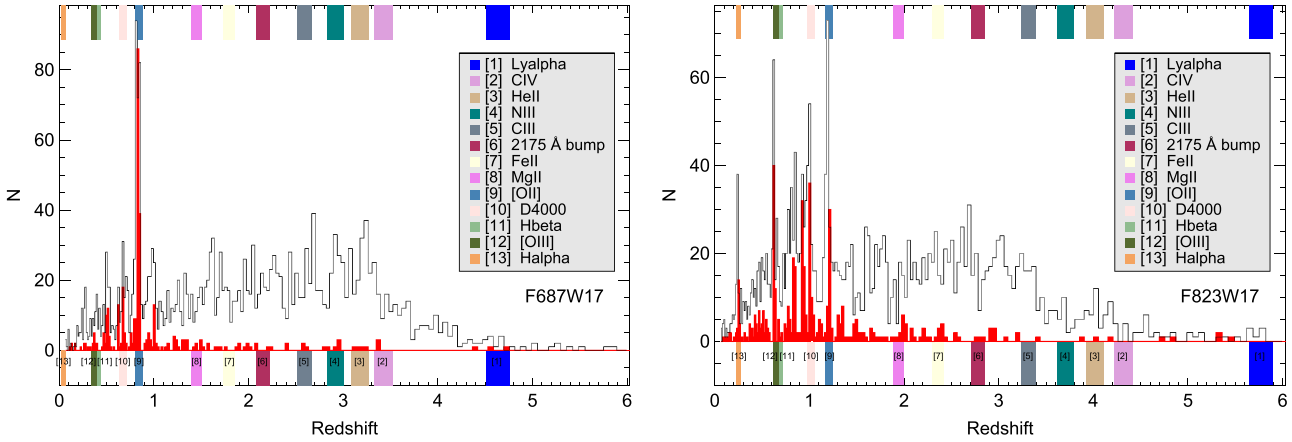

Figure 2. Spectroscopic and photometric redshift distributions for the sources selected as ELG candidates with the F687W17 and F823W17 filters. The histograms in red refer to galaxies with spectroscopic redshift confirmation. The outlined black histograms refer to photometric redshifts (Pérez-González et al. 2008; G. Barro et al. 2015, in preparation). The expected redshifts for emitters with some of the most typical lines (e.g., Lyα, [O II], [O III], or Hα) lying in each one of the two central filters are marked with shaded regions according to the legend of each panel. Numbers below the histogram distributions help to recognize each line. We also mark other spectral features such as the Mg–Fe absorption band at ∼280 nm, or the 2175 Å dust absorption bump, which may mimic emission lines at a different redshift. Bin sizes are proportional to $\Delta(z)/(1+z) \sim 0.006$, our typical photometric redshift accuracy.

Figure 1 shows the selection diagrams for the filters F687W17 (left panel) and F823W17 (right panel). They depict the "continuum-line color" versus the "central-filter magnitude" for each of the two filters. As we move to fainter magnitudes, photometric errors become larger and larger, resulting in a typical "trumpet" shape of the cloud of points. The color versus magnitude distribution can be used to estimate the typical scatter as a function of magnitude. In this plot, σ is the standard deviation of the colors, and we calculate it as a function of magnitude. Galaxies with significantly larger colors than the statistical standard deviation (associated with the photometric uncertainties) are identified as sources with an excess of light in the central filter, i.e., emission-line galaxy candidates. We have chosen a selection function (yellow curve) coming from a 2.5σ cut in the color–magnitude distribution. The vertical orange line represents the minimum detection threshold adopted for the selection, corresponding to the minimum 3σ detection limit of the three filters used in each case (selection band plus the two contiguous filters, see Table 1). These cuts provide a good compromise between inclusion of the largest number of ELG candidates and contamination from spurious sources (see, e.g., Villar et al. 2008, 2011). Summarizing, galaxies identified as potential emitters are found in the *emitters locus* region of these diagrams. Note that the selected galaxies are candidates to have an emission line located in the central filter. This line could be, for the F687W17 filter, [O II] at $z \sim 0.84$, but it may also be any other line such as Lyα at $z \sim 6$ or Hα at $z \sim 0$, among others.

The redshift distributions of the galaxies found in the emitter loci presented in Figure 1 are shown in Figure 2. Most of the peaks in the distribution are actually due to an emission line falling within the observational window of the central filter. Spikes can also be produced by absorption lines and/or breaks in the continuum falling in one of the filters used for the continuum definition, which can mimic an emission line at a different redshift (see Figure 9 in Pérez-González et al. 2013). For example, a number of galaxies can be selected due to the D4000 break (see Hernán-Caballero et al. 2013) falling in the filter used to define the left side of the continuum, mimicking an emission line at lower redshift.

The photometric redshift distribution broadly follows the shape outlined by the spectroscopic sample, revealing their high quality. In Figure 3, we show a comparison between the SHARDS-derived photometric redshifts and available spectroscopic redshifts in the GOODS-N field for our two redshift ranges around $z \sim 0.84$ and $z \sim 1.23$. We have estimated a typical accuracy of $\Delta(z)/(1+z) = 0.006$ by comparison of the photometric redshifts with their corresponding spectroscopic measurements at all redshifts and magnitudes. In the intervals covered by the two filters used in this work, we derived a typical rms ∼0.5%. The high quality of the photometric redshifts is very relevant when aiming at selecting a particular class of ELGs, such as [O II] emitters at two different redshifts, in our case. These photometric redshifts will be presented in another work (G. Barro et al. 2015, in preparation).

For this study, we focus only on the [O II] emitters selected by combining Figures 1 and 2. To make the most robust selection, the tolerance allowed for the inclusion of [O II] ELG candidates is different depending on the type of redshift estimate at hand. Galaxies with already available spectroscopy are easily confirmed as [O II] emitters selected by SHARDS. The selection of galaxies with no spectroscopic confirmation must be done with photometric redshifts, accounting for their uncertainty (see the next section for more details).

2.3.2. *Identification of [O II] Emitter Candidates*

Therefore, the question is how we can identify [O II] emitters and separate them from galaxies with other emission lines or bumps. We identify bona fide [O II] emitters as those ELG candidates for which the spectroscopic redshift is such that the [O II] line lies within the interval implicitly defined by the FWHM of the observed central passband. Note that, as explained in Section 2.3 and Pérez-González et al. (2013), the actual passband seen by each galaxy depends on the exact position in the GTC/OSIRIS FOV. The procedure is explained graphically in Figure 4. The medium-band technique is very effective in selecting ELGs in a narrow range of redshifts. If we had spectroscopic confirmation for all sources, those ranges would be as narrow as $\Delta(z) \sim 0.05$. However, ∼53% of galaxies finally identified as [O II] emitters at $z \sim 0.84$ and

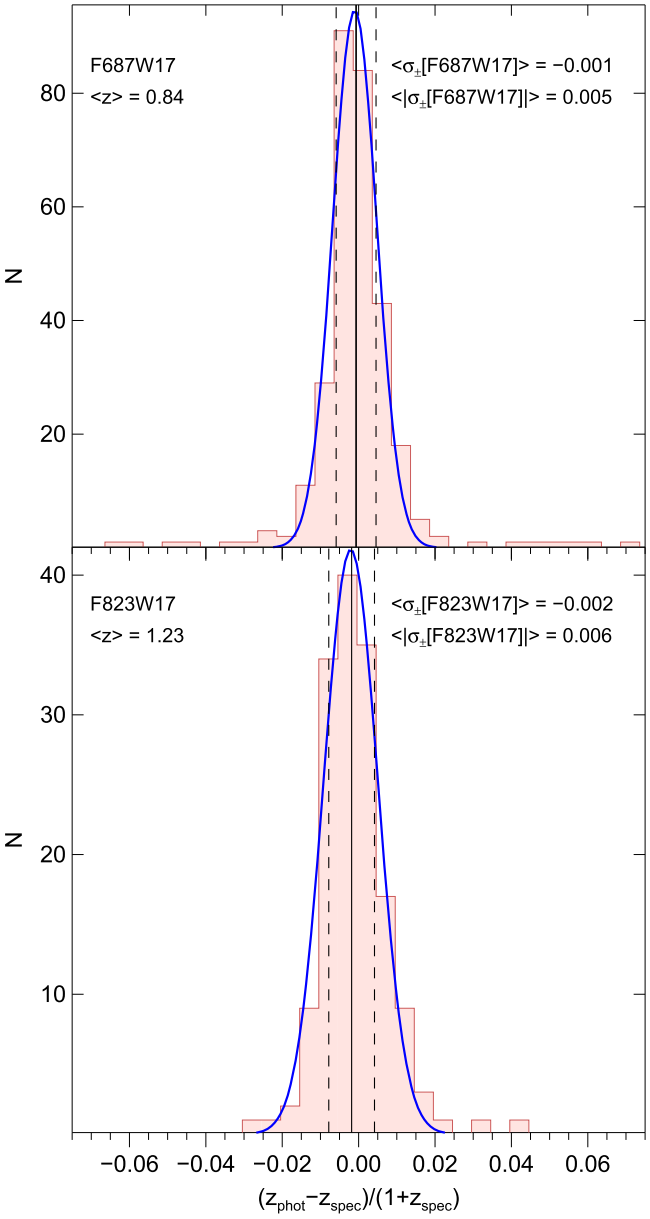

Figure 3. Comparison between spectroscopic and photometric redshifts for SHARDS sources around $z \sim 0.84$ (top panel) and $z \sim 1.23$ (bottom panel), the two redshifts where we present [O II] emitters selected with the F687W17 and F823W17 filters. We show the distributions of redshift accuracies, $\sigma_{\pm} = (z_{\rm phot} - z_{\rm spec})/(1 + z_{\rm spec})$. In both panels, the blue curve is the Gaussian fit to the distribution, with the vertical solid and dashed lines representing the mean offset and 1σ dispersion respectively.

$\sim$74% of the sample $z \sim 1.23$ count only on a photometric redshift. In order to determine which galaxies are actual [O II] emitters on the basis of photometric redshifts, we have to consider the error of those photo-z's.

In addition to this, due to the variable central wavelength (CWL) along the FOV of the OSIRIS instrument, we obtain a continuum distribution for the selection function that depends on the CWL of the filter for each galaxy position. Combining all effects, we obtain the hatched region in Figure 4, which represents the overall extent in the redshift space for our selection function based on the *trumpet* plots in Figure 1 and the photometric redshifts (see Figure 2). We remark that this redshift range does not apply to the selection in the whole area surveyed by SHARDS: the redshift range probed actually depends on the position of the galaxy in the FOV.

This procedure provides two catalogs of ELGs selected as [O II] emitters based on the two redshift estimates: one using photometric redshifts, and one on the basis of spectroscopic redshifts, which should be a subsample of the former. We call the latter the spec-z-confirmed ELGs, while the former is the photo-z-selected sample. These catalogs can be merged to get a robust and complete selection. Adopting a similar procedure, we are able to produce catalogs for each possible detected line (such as those listed in the legend of Figure 2) and we plan to analyze the full combined set of detected lines in a future work.

In order to assess and improve the selection of [O II] emitters, we compare the spectroscopic and photometric selected samples in Figure 5. In the top panels, we plot the redshift distribution of the two samples of [O II] emitters based on spectroscopic and photometric redshifts. The photometric redshift selection closely follows the spectroscopic distribution, but it includes a higher number of galaxies. If the galaxies selected with photometric redshifts are bona fide [O II] emitters, then half of the $z \sim 0.84$ sample and a quarter of the $z \sim 1.23$ sample currently would have a spectroscopic confirmation (i.e., the spectroscopic completeness is $\sim$50% and $\sim$25%).

It is interesting to note that the galaxies with no spectroscopic confirmation are typically fainter than AB ~ 24.5, as clearly shown in Figure 1. In fact, the spectroscopic completeness for the selected bona fide [O II] emitters brighter than $R = 24.5$ is $\sim$91% (74%) in the F687W17 (F823W17) filter, and $\sim$13% (16%) for galaxies with $R > 24.5$ mag. This is the spectroscopic limit of the redshift surveys carried out in the GOODS-N field, and the typical detection threshold for the vast majority of data taken with state-of-the-art spectrographs in 10 m class (or smaller) telescopes. The SHARDS observations reach at least 2 mag fainter, and thus make it possible to reliably select and study fainter and/or higher redshift ELGs. We note, furthermore, that the number of galaxies having publicly available spectra of good quality, where the signal-to-noise ratio (S/N) is sufficiently high to derive a robust EW and [O II] line flux determination, represents only a small fraction (typically $\sim$5%–10%) of the total number of galaxies for which a spectroscopic redshift determination is available in this study.

In the second and third rows of Figure 5, we compare more quantitatively the samples selected with spectroscopic and photometric redshifts in terms of the success rate and the contamination. The success rate is defined as

$$\mathrm{SR} = N_{\rm ph-conf}/N_{\rm sp} \quad (1)$$

where $N_{\rm sp}$ is the number of galaxies in the spectroscopic catalog and $N_{\rm ph-conf}$ is the number of galaxies with a spectroscopic confirmation that are included in the photometric redshift sample. This number is related to the ability to select a galaxy using the photometric redshift and provides an estimate of the number of galaxies we lose due to uncertainties in the photo-z or a failure in the detection of the emission line with the SHARDS filter. Typically, the selection based on SHARDS medium-band data and photometric redshifts has a success rate higher than 90%.

In an analogous way, we define the contamination as

$$C = 1 - N_{\rm ph-conf}/N_{\rm ph-sp} \quad (2)$$

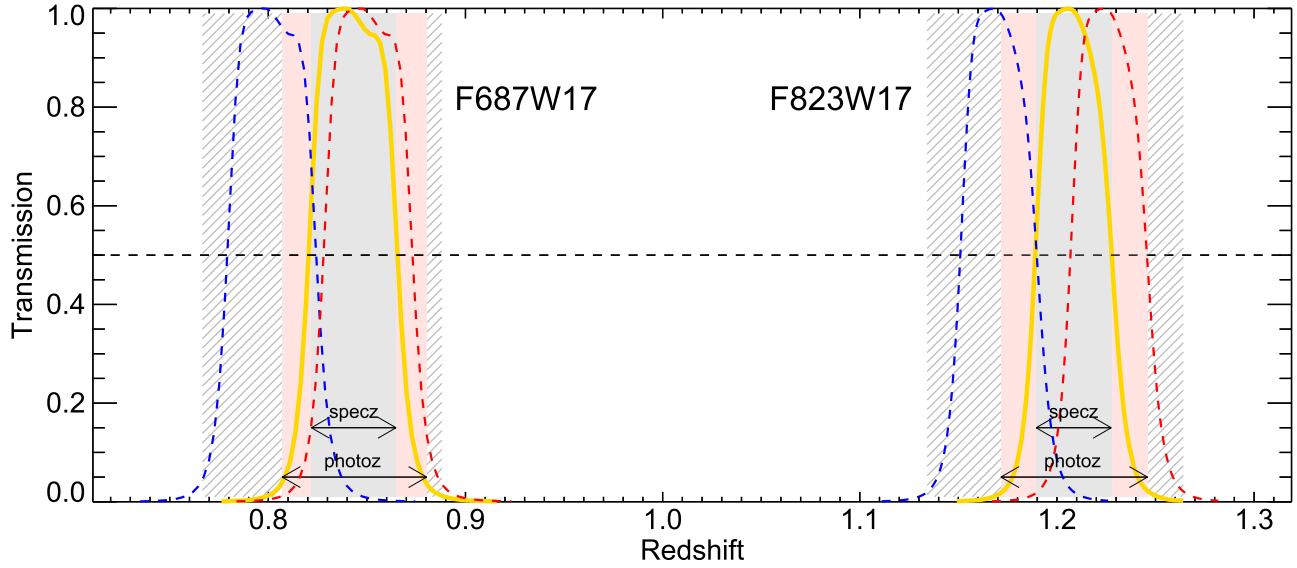

Figure 4. Scheme of the redshift dependence of the selection of [O II] ELGs based on the SHARDS medium-band data. We show the results for filters F687W17 ($z \sim 0.84$) and F823W17 ($z \sim 1.23$). Blue (red) dashed lines show the transmission curves for the bluest (reddest) passbands seen by any galaxy in the SHARDS images for these filters. The orange curves represent the nominal central passband for the given SHARDS filter (centered on 687 and 823 nm). The filled gray area represents the interval where galaxies with spectroscopic redshifts are selected. The shaded pink area indicates the redshift interval of the selection for galaxies with photometric redshifts. Its width is based on the mean error of the photometric redshift $\langle \delta(z) \rangle = \sigma \times (1 + z)$ at redshift z, where $\sigma = 0.005$ for $z \sim 0.84$ and $\sigma = 0.006$ for $z \sim 1.23$. The 50% normalized transmission is marked with a black dashed line. The gray-hatched area gives the global envelope of the transmission curves along the FOV.

where $N_{\rm ph-sp}$ is the total number of galaxies in the photometric catalog having a spectroscopic redshift estimate (either within the expected redshift range or outside). This number gives an estimate of the fraction of contaminants expected in the final sample. The contamination measured in both redshift bins considered in our study is less than 10%. The measured success rate and contamination level are consistent with the expectations due to the photometric redshift errors and spectroscopic uncertainties for the faintest observed galaxies.

In the bottom panels of Figure 5, we show the redshift distribution for the final sample of bona fide [O II] emitters built by merging the samples selected on the basis of spectroscopic and photometric redshifts. These final catalogs do not include the known contaminant galaxies identified on the basis of measured spectroscopic redshifts. Accounting for this, the final contamination fractions are 2% and 6% for the filters F687W17 and F823W17, respectively. Obviously, both the contamination and the success rate for the final selection are very sensitive to the photometric redshift errors. We have verified the effect of using photometric redshift catalogs derived using only broad-band photometry (that is, excluding SHARDS data), with an accuracy of $\Delta(z)/(1 + z) \sim 0.03$, typical of most photometric redshift catalogs. The success rate decreases to ∼70% level, and the contamination increases to ∼40%. Henceforth, we will always refer to the sample shown in the bottom panels of Figure 5 as the final [O II] emitter sample.

2.4. Complementary Samples: Mass-selected, IR-detected, and Quiescent Galaxies

As already mentioned before, we use in our analysis the ancillary multi-wavelength catalog and advanced products in the GOODS-N field presented in Pérez-González et al. (2008) and compiled in the Rainbow Cosmological Surveys Database (see Pérez-González et al. 2008; Barro et al. 2011a). This data set includes observations from X-rays to the far-IR and radio bands, as well as spectroscopic data in the GOODS-N field from the literature. In Pérez-González et al. (2008), we presented a merged photometric catalog including broad-band data for a stellar mass-selected sample based on ultra-deep IRAC observations. For this work, we have merged this catalog with the SHARD data set. As described in Pérez-González et al. (2008), the parent sample used in this paper has been built using IRAC luminosities as proxies for the stellar mass. Thanks to the ultra-deep IRAC imaging available, our sample is mass-complete for galaxies with $M > 10^9 M_\odot$ up to redshift $z = 1$.

In order to perform a comprehensive study of SFGs at $z \sim 0.84$ and $z \sim 1.23$, we have built a general parent sample, starting from the GOODS-N mass-selected sample, by selecting all the galaxies that would enter the medium-band filter selection using the SHARDS data (i.e., with the same redshift distribution as our [O II] emitters), independently from their emission properties.

We apply the same selection procedure presented in Section 2.3.2 for the selection of [O II] emitters, but this time relaxing the condition on the emission properties of the galaxies. This means that the position-dependent redshift selection function (as schematically represented in Figure 4) will not be applied only to the ELG candidates (i.e., galaxies within the *emitter locus* in Figure 1) but to the whole mass-selected galaxy sample, independently of the emission properties. In other words, we check the position within the FOV of each galaxy selected from its (photometric or spectroscopic) redshift, and then determine whether that redshift is good for a selection based on the SHARDS filters should the galaxy have an emission line. In this way we can define a parent sample that includes and complements our [O II] emitter compilation and provides a complete census of galaxies (both star-forming and

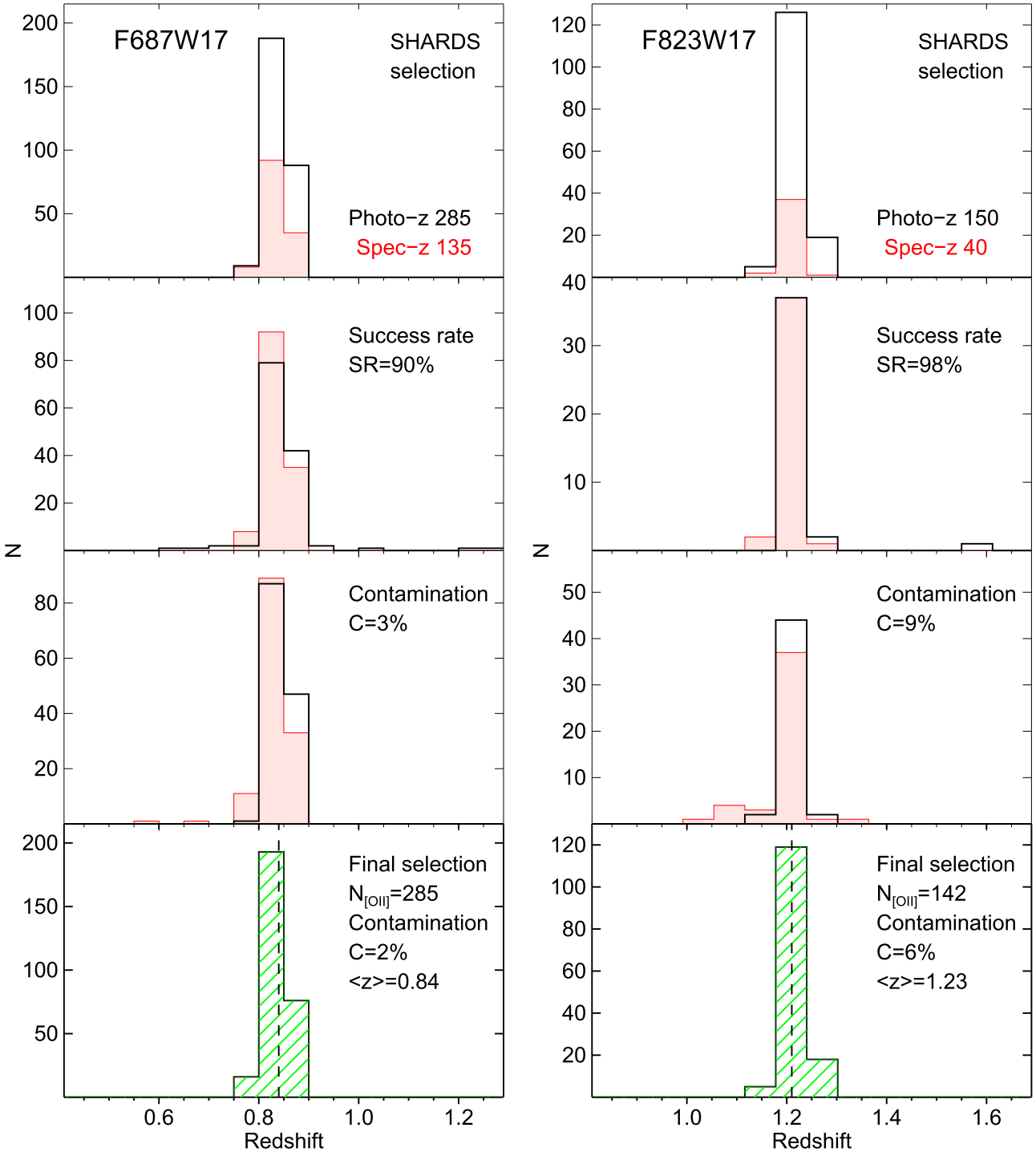

Figure 5. Redshift histograms showing the selection, success rate, and contamination rate for the [O II] ELG candidate samples built with central filters F687W17 ($z \sim 0.84$, left plots) and F823W17 ($z \sim 1.23$, right plots) using spectroscopic or photometric redshifts. Top panels: redshift distributions for the selected objects using spectroscopic (red filled histogram) or photometric (black histogram) redshifts. Second row of panels: redshift distribution of objects selected on the basis of their spectroscopic redshift (red filled histogram) compared to the photometric redshift distribution for the same galaxies (black histogram). The ratio in the numbers of objects in these distributions defines the *success rate* (SR). Third row of panels: redshift distribution for objects selected on the basis of their photometric redshift (black histogram) compared to the distribution of their corresponding spectroscopic redshifts (red filled histogram) for those objects in which both redshift estimates are available. The normalized difference in the numbers of objects in these distributions defines the *contamination* (*C*). Bottom panels: redshift distribution for the final selected sample built by complementing the spectroscopic and photometric redshift selections. The vertical dashed line represents the median redshift in each panel.

quiescent) at those redshifts, which we simply dub the *parent sample* hereafter.

Starting from this general selection, we can derive different subsamples according to several indicators for the SFR. In fact, we can estimate the SFR from the rest-frame UV luminosity (corrected for attenuation) derived from the SED fitting for all the parent sample, then we can define the subsamples of [O II]-detected (according to our SHARDS selection) and IR-detected galaxies (for example, using *Spitzer*/MIPS 24 μm data). Finally, we can define a sample of quiescent galaxies using the rest-frame $(V - J)$ versus $(U - V)$ color–color diagrams following Whitaker et al. (2011), or alternatively as all galaxies lying below a certain

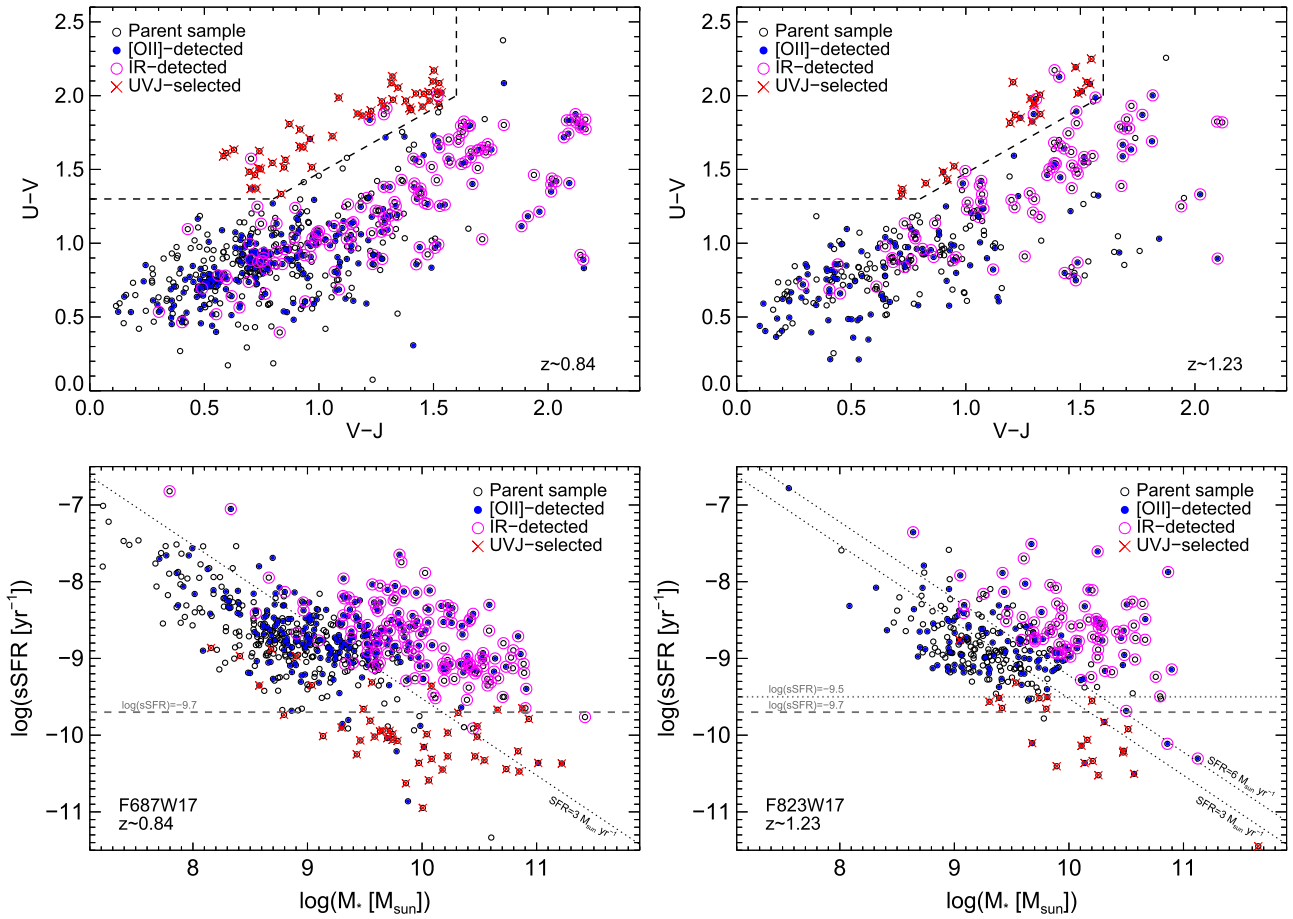

Figure 6. Top panels: *UVJ* color–color diagram with the region of quiescent galaxies defined as in Whitaker et al. 2011 (F687W17 to the left, F823W17 to the right). IR-detected galaxies within the *UVJ* quiescent region are excluded from the passive sample. The different samples are indicated with different symbols identified in the legend. Bottom panels: sSFR–M_* diagrams for the two SHARDS filter selections at $z \sim 0.84$ (left panel) and $z \sim 1.23$ (right panel). The different subsamples are plotted with different symbols identified in the legend. *UVJ*-passive galaxies are defined as in Whitaker et al. (2011). The dark-gray dashed and dotted horizontal lines mark two cuts at constant sSFR (log(sSFR [yr^{-1}]) = −9.7 and −9.5), adopted for the sSFR-based definition of quiescent galaxies. The black-dotted lines mark the sSFR–M_* relations for constant values of SFR (SFR = 3 and 6 $M_\odot$ yr^{-1}), corresponding approximately to our detection limits for IR-selected galaxies in the two redshift ranges.

specific SFR (sSFR) cut (we use 0.2 Gyr^{-1} as our arbitrary limit) and not presenting IR emission.

Interestingly, the sample of quiescent galaxies defined on the basis of their sSFR does not fully overlap with the definition of *UVJ*-passive galaxies usually adopted in the literature (Whitaker et al. 2011), although relaxing the cut in sSFR would improve the agreement, especially for the higher redshift sample. In fact, increasing the cut from log(sSFR [yr^{-1}]) = −9.7 to log(sSFR [yr^{-1}]) = −9.5 (shown as horizontal dashed and dotted dark-gray lines in the bottom panels of Figure 6 respectively), the fraction of commonly selected objects would rise from ∼55% to ∼85% for the $z \sim 1.23$ sample. Hereafter, we will use "quiescent sample" to refer to the one selected on the basis of the *UVJ* diagram, unless stated otherwise. Summarizing, the number of galaxies in each sample is 585/285/143/47 and 332/142/83/21 for the comparison/[O II]/IR/*UVJ* subsamples in the F687W17 and F823W17 filters respectively. The definition of the samples is illustrated in Figure 6. We observe also that our IR detection limit is SFR ~ 3 $M_\odot$ yr^{-1} and SFR ~ 6 $M_\odot$ yr^{-1} for the F687W17 and F823W17 filters respectively. We mark these constant-SFR relations as black-dotted lines in Figure 6.

In Figure 7, we show the spectroscopic and photometric redshift distributions for the total population of galaxies in GOODS-N extracted from the Rainbow Database. We compare this global distribution with the redshift distribution of bona fide [O II] emitters identified through the two SHARDS filters used in this work (see Section 2.3.2) and with the parent sample defined above. From this figure we notice that in the case of filter F687W17, corresponding to the redshift slice at $z \sim 0.84$, we are selecting our [O II] emitters from a large-scale overdense region, clearly identified by the global spectroscopic (and also photometric) redshift distribution. Note also that the photometric and spectroscopic redshift distributions closely agree, confirming the goodness of photometric redshift estimates.

2.5. AGN Fraction

Our method to detect ELGs is sensitive to both SFGs and AGNs. Since we are interested in the former, we discuss here the possible contamination from AGNs in our sample. Of course, these AGNs likely also have active SF.

The SHARDS field fully overlaps with the 2 Ms CDFN (Alexander et al. 2003). The X-ray source catalog from Alexander et al. (2003) contains 267 X-ray sources in the area surveyed by SHARDS. The Chandra images are deep enough to detect the X-rays associated with normal SF (e.g., Persic et al. 2004; Lehmer et al. 2010; Pereira-Santaella et al. 2011).

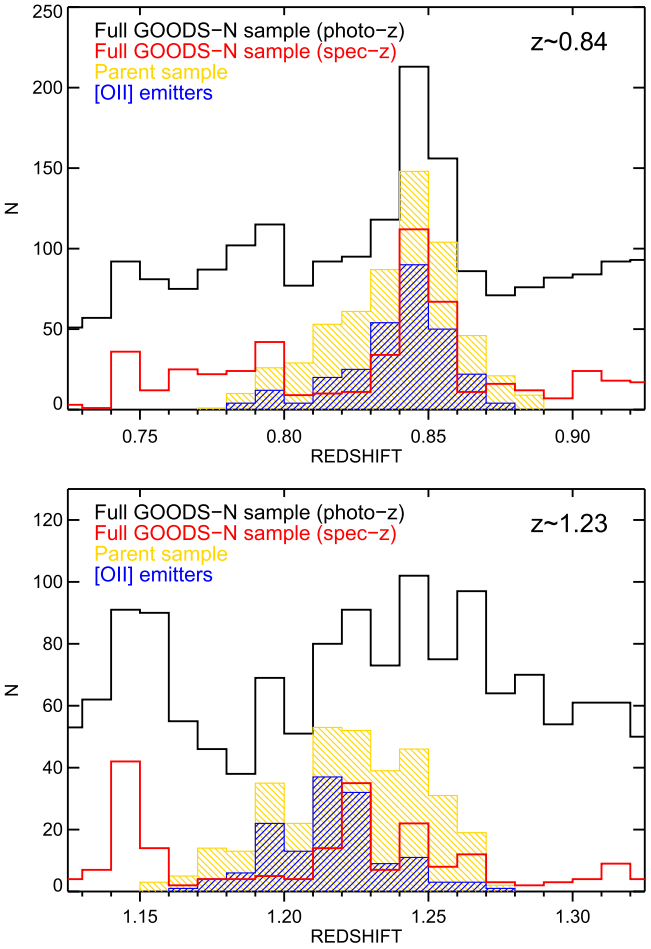

Figure 7. Histograms illustrating the redshift distributions for the selected sample of the [O II] emitters (blue shaded histogram) and the parent sample (yellow shaded histogram) extracted from the parent catalog by applying the same filter selection function. For completeness, the photometric and spectroscopic redshift distributions for the parent catalog are also shown (black/red outlined histograms respectively). Note that for the lower redshift selection (upper panel) the presence of a prominent large-scale structure is evident.

In order to avoid contamination from non-AGN X-ray sources, we restrict our AGN identification to sources with X-ray luminosities $L_X > 10^{42}$ erg s^{-1} from Barger et al. (2008) in either the soft (0.5–2 keV) or hard (2–8 keV) band. Cross-matching our samples of [O II] emitters with the ultra-deep X-ray CDFN catalog, we identify four AGNs in the F687W17 sample at $z \sim 0.84$ and two AGNs in the F823W17 sample at $z \sim 1.23$. These numbers correspond to a fraction of $\sim$1.2% of the samples, values in good agreement with the X-ray-selected AGN fraction of 1%–2% estimated by Zhu et al. (2009) in their analysis of $z \sim 1$ [O II] emitters in the DEEP2 survey. Ciardullo et al. (2013) found a slightly higher fraction of AGNs ($\sim$3%) from their sample of [O II]-selected galaxies in the HETDEX pilot survey (Hill et al. 2008; Adams et al. 2011), although they used a fainter limit for identifying AGNs from the parent X-ray catalog. As mentioned above, the correlation between X-ray emission and AGN contribution to the derived SFR does not necessarily imply that the integrated [O II] emission is dominated by flux from the central engine. However, the SFR estimations based on indicators such as the [O II] emission could be contaminated by the AGNs. Indeed, by examining the few X-ray-bright objects in our survey we verified that these candidate AGNs are generally not among the strongest [O II] emitters. The uncertainty of the contribution of the AGNs to the observed [O II] emission and the small number of objects involved lead us to conclude that the exclusion of candidate AGNs from the final sample constitutes a negligible source of uncertainty in our results. We note that a small fraction of highly obscured AGNs could be missed by selecting only on the basis of the observed X-ray emission, which is able to select mostly unobscured and moderately obscured AGNs (see, e.g., Fiore et al. 2009, 2012). However, given the extreme depth of the available X-ray data in the GOODS-N field, and the already modest fraction ($\sim$1%) of unobscured + moderately obscured AGNs detected in our sample, we can assume that the additional number of highly obscured AGNs is negligible.

3. OBSERVATIONAL PROPERTIES OF THE [O II] EMITTER SAMPLE

In this section, we describe the procedure to measure [O II] fluxes and EWs from the SHARDS data for the [O II] sample of galaxies described in the previous section. The method is based on the estimation of the continuum emission around the emission line by comparing the SHARDS spectro-photometric data with stellar population models, and then using the central filter to measure the line flux. This modeling is described in Section 2.2. Then we compare the properties of our [O II] emitters with other similar samples from the literature.

3.1. Line Fluxes and EWs of [O II] Emitters

For the final samples of [O II] emitters at $z \sim 0.84$ and $z \sim 1.23$ selected from the F687W17 and F823W17 filters, we have measured line fluxes and EWs using the SHARDS medium-band data as detailed next.

The flux emitted in the [O II] line is by definition (see, e.g., Villar et al. 2008; Sobral et al. 2012)

$$F([\mathrm{O\,II}]) = \left(f_\lambda^{\mathrm{central}} - f_\lambda^{\mathrm{continuum}}\right) \times \Delta\lambda^{\mathrm{central}} \quad (3)$$

where $f_\lambda^{\mathrm{central}}$ and $f_\lambda^{\mathrm{continuum}}$ are the measured flux densities in the central filter containing the emission line and the continuum obtained from the stellar population fits (defined as described below in this section). $\Delta\lambda^{\mathrm{central}}$ is the FWHM of the SHARDS central filter. The derived observed EW is

$$\mathrm{EW}([\mathrm{O\,II}]) = F([\mathrm{O\,II}]) / f_\lambda^{\mathrm{continuum}} \quad (4)$$

where $F([\mathrm{O\,II}])$ is the line flux defined above.

We have followed a careful and sophisticated method to measure EWs and fluxes, based on a robust determination of the continuum around the emission line. The continuum estimation can be extracted from a linear interpolation between the two continuum filters used in the selection of ELG candidates, but this method can be affected by line contamination of the side filters or other local features. A more accurate estimation relies on the use of stellar population models fitting the medium-band data around the emission line (see, e.g., Díaz-García et al. 2015; Vilella-Rojo et al. 2015, for a similar approach), thus exploiting all the information available from the SHARDS data.

In Figure 8, we illustrate the adopted procedure for a galaxy at $z \sim 0.84$. The SHARDS data are fitted to stellar population synthesis models as described in Section 2.2. When performing the fit, we excluded the filter containing the emission line,

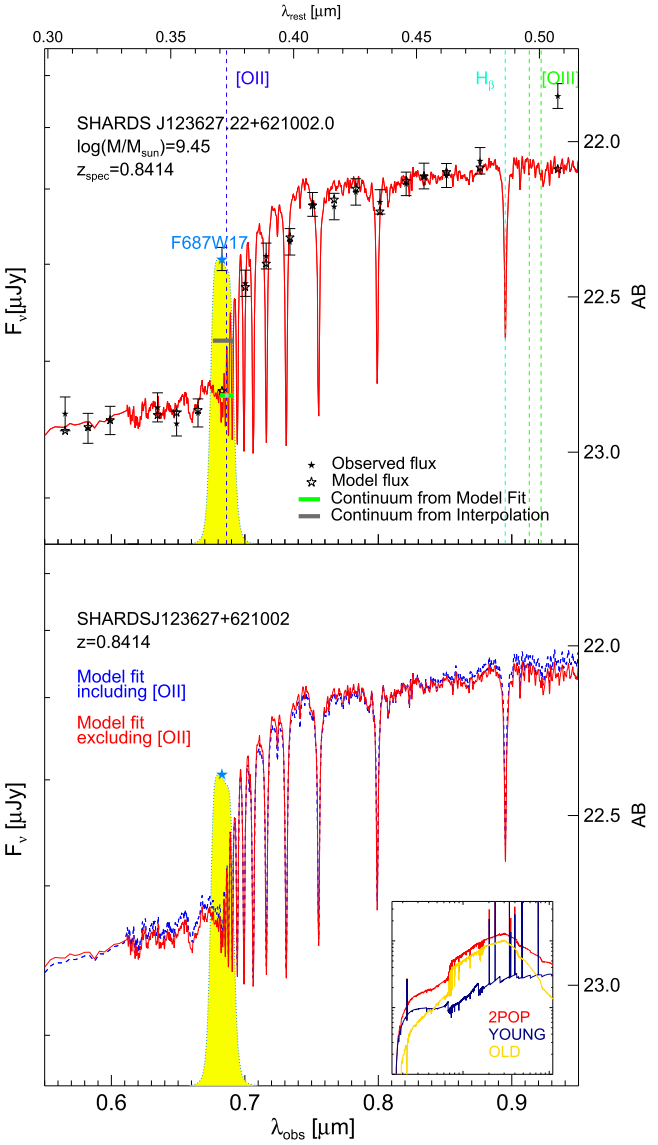

Figure 8. Illustration of the method used to refine flux and EW measurements from SHARDS data by determining an accurate continuum level (upper panel) for [O II]. For all the galaxies selected as [O II] emitters, we fit the SHARDS medium-band data to stellar population models and extract the continuum level from the best fitting model. Black filled stars are the SHARDS medium-band observed fluxes (with the associated 1σ error bars), with the larger blue star indicating the filter used for the detection of the [O II] emission line. In red, we show the best-fit model to the SHARDS data (see text for details). Open stars represent the flux predicted from the best-fit model, after convolution with the SHARDS filters. We mark with a horizontal gray segment the continuum obtained by simple interpolation of the two adjacent filters to the central passband. The continuum obtained from the best-fit model is marked in green. We also illustrate (lower panel) the effect of excluding (continuous red line, same as in the upper panel) or including (dashed blue line) the photometric data point corresponding to the filter containing the [O II] line. The small inset shows the global two-population fit (in red) depicted in the two main panels, with the young/old components overplotted in blue/yellow respectively.

which is obviously contaminated. The model allows us to determine the continuum at the position of the emission line. The continuum obtained from the best fit (green segment in Figure 8) is usually lower (on average ∼10%–15% lower density flux) than that obtained from the linear interpolation (gray line) of the two adjacent filters. This translates into a systematically larger (but more robust) EW for the line (on average ∼35%–40% larger EWs) and higher fluxes (on average ∼25%–30% larger fluxes). In the lower panel of Figure 8, we show the effect of including or excluding the filter that contains the emission line. Typically, there is not much difference between the two fits (<10% difference in derived EW), but larger discrepancies (up to ∼50% difference in derived EW) can be found when the emission line is very strong, affecting the continuum determination.

In order to assess the reliability of our measurements based on spectro-photometric data from SHARDS, we compare line fluxes derived from our medium-band filters with those derived from spectra of the same objects and available from the literature (TKRS, Wirth et al. 2004, and DEEP3 data, Cooper et al. 2011). The subsample of galaxies having spectra of good quality, i.e., S/N high enough to robustly measure EW([O II]) and F([O II]), contains 42 galaxies (∼10% of the final sample). We show the comparison between the line fluxes measured on the basis of the publicly available spectroscopic and SHARDS photometric data in Figure 9.

On average, fluxes measured from spectroscopy are ∼30%–35% larger than fluxes measured from SHARDS photometry when using a continuum determined from linear interpolation between adjacent filters. Our procedure to estimate the continuum based on stellar population synthesis models significantly improves the comparison between spectroscopic and photometric line fluxes, making them consistent within ∼5%–10%. Despite the large scatter, this result supports the robustness of our approach. Note that the spectroscopic measurement of the line flux is affected by slit losses, and typically this correction is carried out by assuming that the whole galaxy has a constant EW equal to the one measured in the spectra. If galaxies count with nuclear bursts, this correction would overestimate the total flux of the galaxy. This is confirmed by Figure 9, where we show that the observed EW ([O II]) from SHARDS data are, on average, ∼30% smaller than those measured in spectra. In contrast, photometric measurements of the line flux using integrated magnitudes are not affected by aperture effects, although spatial gradients of the emission could affect the selection of ELG candidates.

We show the resulting distribution of rest-frame EWs (EW_{rf}([O II])), F([O II]), and R-band magnitudes for the final sample in Figure 10. Errors in the estimates of the line flux and continuum level propagate into uncertainties in the derived EW_{rf}([O II]) of ∼20% at most. We observe a median (and [quartiles]) rest-frame EW_{rf}([O II]) = 51[38, 65] Å at $z \sim 0.84$ and EW_{rf}([O II]) = 67[49, 91] Å at $z \sim 1.23$. A shift of ∼0.5 mag is also seen in the observed R-band magnitude distribution, with the higher redshift sample peaking at fainter magnitudes. The line flux distribution is similar in the two cases, ensuring that we are not introducing any particular redshift-dependent bias in line flux measurements. The median observed line flux for both distributions is $\sim 2 \times 10^{-17}$ erg s^{-1} cm^{-2}, with measurements extending to $\sim 2 \times 10^{-18}$ erg s^{-1} cm^{-2} on the faint end. We note that the minimum rest-frame EW achievable assuming the typical uncertainty for the faintest [O II]-selected galaxies corresponds to 30 and 36 Å for the higher and lower redshift samples respectively. For brighter galaxies with smaller uncertainties we can reach even smaller values for the EW. The smaller value for the higher redshift sample is due to the smaller rest-frame filter width at this redshift. These values are indicated as a dotted–dashed vertical blue line in the left panels of Figure 10. These lower limits ensure a robust determination of the median EW_{rf}([O II]) values discussed in the following section. Indeed, we can convert these values to a

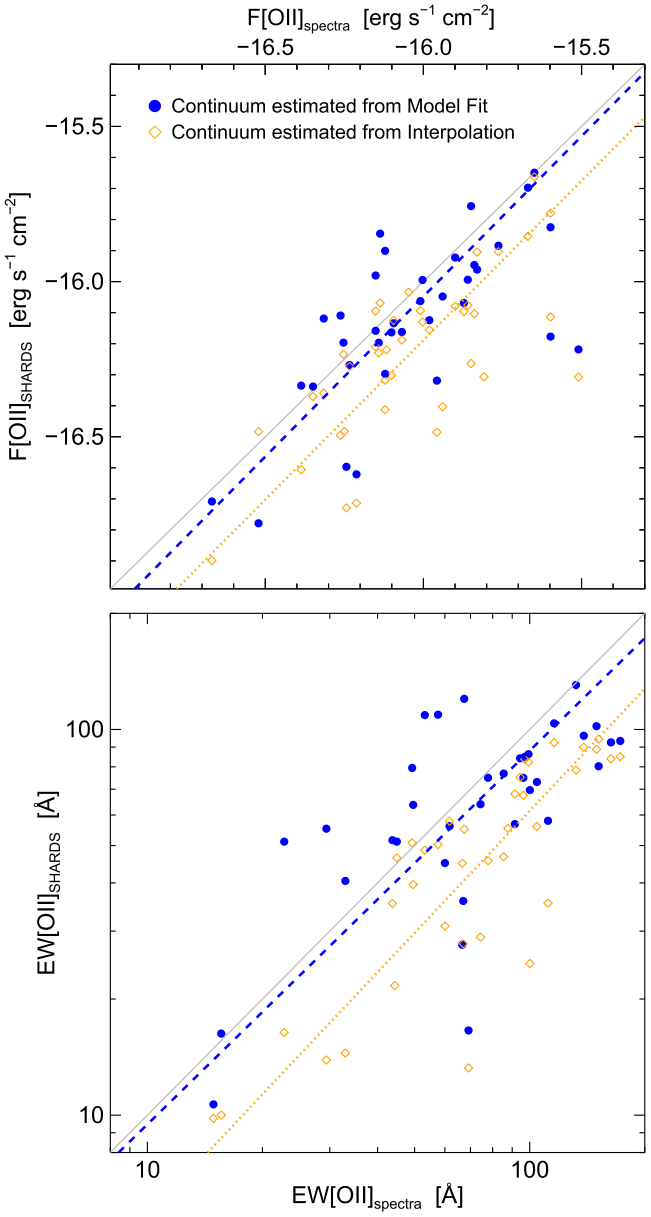

Figure 9. Comparison between spectroscopic and SHARDS-derived line fluxes and EWs for the [O II] line (upper and lower panels respectively). Spectroscopic measurements are obtained from public data (TKRS and DEEP3 spectra). The continuum gray line represents the identity relation. Blue points and orange diamonds represent flux and EW estimates based on best-fit or linear interpolation for the continuum, respectively. The blue-dashed and orange-dotted lines are the linear best fit to the two data sets.

lower limit in the line-flux detection ($F([\mathrm{O\,II}])_{\mathrm{limit}} \sim (6\text{–}8) \times 10^{-18}$ erg s^{-1} cm^{-2}), also reported as a vertical blue dotted–dashed line in the central panels of Figure 10. In this case, as expected, a slightly higher observed line flux limit is found for the higher redshift sample.

These flux and EW detection limits are comparable to those obtained with deep spectroscopy. We conclude that our SHARDS spectro-photometric survey is very effective in selecting ELGs down to the faintest flux levels achieved by spectroscopy. Note that the median fluxes and EWs of our samples are significantly higher than the detection limits, so the results presented in the following sections are not significantly affected by incompleteness at the faintest flux or smallest EW levels.

3.2. EW_{rf}([O II]) Evolution

The measurement of the EW([O II]) provides a valuable source of information on the relevance of the ongoing SF in galaxies. As is well known (e.g., Kennicutt 1998) the [O II] line flux is strictly related to the radiation field coming from the young ($t < 20$ Myr) and massive ($M > 8\ M_{\odot}$) stellar populations (and also to metallicity and other properties such as density and temperature). On the other hand, the continuum is more representative of SF on a longer timescale ($t \sim 1$ Gyr). The ratio of these quantities, i.e., EW([O II]), thus provides an estimate of the current SF efficiency at the epoch of observations with respect to the average SF in the past life of the galaxy. This is an indicator of the current SF efficiency of the galaxy and it is largely independent of the degree of internal extinction of a galaxy.

In some recent works (see, e.g., Kornei et al. 2012; Lee et al. 2012; Ly et al. 2012; Ciardullo et al. 2013) the distributions of the EWs for large samples of [O II] ELGs are presented and their median values given for samples ranging from $z = 0$ to $z \sim 1$. Locally, the distribution of rest-frame EW ([O II]) for [O II]-selected galaxies is known to peak near 5 Å, and then it rapidly decays without any noticeable dependence on the galaxy luminosity (Blanton & Lin 2000).

In Figure 11 we show the evolution of the median $\mathrm{EW_{rf}}$([O II]) measurements of [O II]-selected samples from the literature at redshifts $0 < z < 1.5$ compared to the values obtained for our SHARDS emitters. Our estimates of $\mathrm{EW_{rf}}$([O II]) are consistent with those derived by other authors at similar redshifts (compare them with those from Kornei et al. 2012 and Teplitz et al. 2003 in the figure), meaning that our technique based on medium-band data does not include any systematic bias on these measurements and provides robust EW values.

The $\mathrm{EW_{rf}}$([O II]) evolution curve appears to rise as $\sim(1 + z)^3$ up to $z \sim 1$, and then flattens or starts to decrease at higher redshifts. We interpret this as a real decrement presented by the $\mathrm{EW_{rf}}$([O II]) evolution curve. In fact, the global behavior of the evolution of $\mathrm{EW_{rf}}$([O II]) with redshift appears to follow that of the SFR density (SFRD) of the universe (see, e.g., Madau & Dickinson 2014 for a recent review), presenting a steep rise (proportional to $\sim(1 + z)^{\alpha}$, with $\alpha \sim 3.2$), up to $z \sim 1$ and a flattening (or slow decline) at higher redshift (as suggested by the measurements at $z \sim 1.5$ from Ly et al. 2012). Indeed, the value of the slope α is quite similar to those derived from SFRD studies, where values between 3 and 4 are usually obtained (e.g., Lilly et al. 1996; Baldry & Glazebrook 2003; Pérez-González et al. 2005; Tresse et al. 2007, 2002; Cucciati et al. 2012). This trend reflects the varying SF efficiency at different epochs in the life of the universe, which is well traced by such a simple quantity as the EW of [O II] emitters.

4. PHYSICAL PROPERTIES OF THE [O II] EMITTERS AT $z \sim 0.84$ AND $z \sim 1.23$

In this section, we discuss and compare the SFR, stellar mass, and (mass-weighted) age properties of the [O II] ELGs selected in the redshift bins identified by our two SHARDS

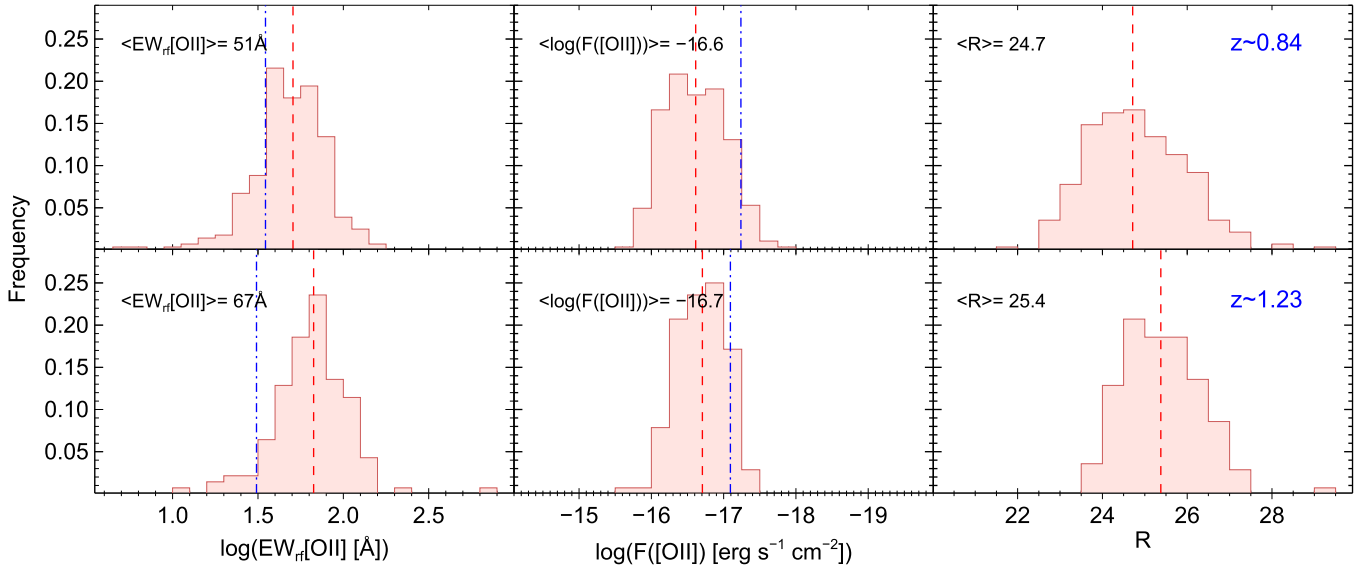

Figure 10. Distributions of EWs, line fluxes, and *R*-band magnitude for the [O II]-selected galaxies at $z \sim 0.84$ (upper panels) and $z \sim 1.23$ (bottom panels). The vertical dashed lines represent the median values also given in each panel. The blue dotted–dashed line in the left and central panels marks the minimum EW_{rf}([O II]) and corresponding flux achievable assuming the typical uncertainty for the faintest galaxies in our sample.

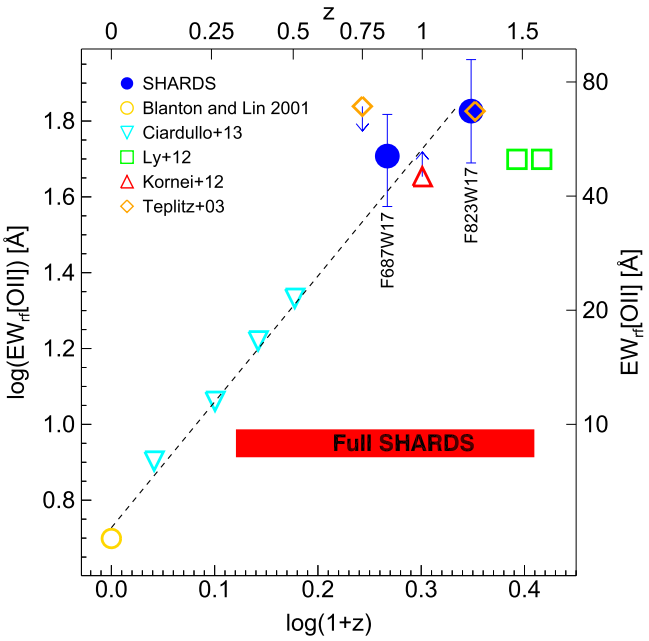

Figure 11. Evolution of the median EW_{rf}([O II]) with redshift. We represent the values derived in this study for $z = 0.84$ and $z = 1.23$ and a compilation from the literature at different redshifts up to $z \sim 1.5$ (see the legend). The dashed line represents the best fit in the form $EW_{rf}([O\,II]) \sim (1+z)^{\alpha}$, with $\alpha = 3.2$. The arrows indicate upper or lower limits respectively (see text for details). The datum at $z \sim 0.75$ from Teplitz et al. (2003) should be considered as an upper limit since their detection limit does not allow them to measure EWs lower than ∼35 Å. The point from Kornei et al. (2012) should be considered as a (slightly) lower limit since their EW distribution is biased toward higher mass objects ($\langle M \rangle \sim 1.5 \times 10^{10} M_{\odot}$). The data from Ly et al. (2012) show a lower value (∼50 Å) of the median EW measured for their two redshift bins at $z \sim 1.47$ and $z \sim 1.62$ with respect to the trend presented in the lower redshift bins. These last points are not included in the fit, because they may represent a flattening of the EW_{rf}([O II]) evolution at $z > 1$.

filters. In the following section we will compare the properties of [O II] emitters with the other subsamples defined in Section 2.4, investigating the effect of using different SFG selection techniques.

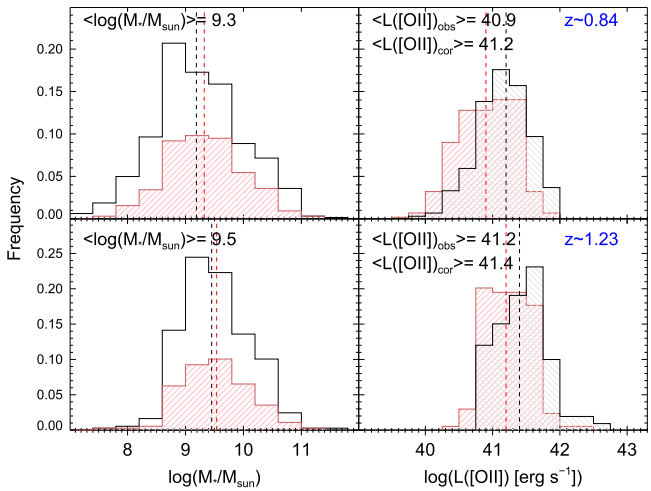

Figure 12. Left panels: distribution of stellar masses for the [O II] emitters (hatched histogram) and the parent sample (black outlined histogram). Vertical dashed lines indicate the median value for the [O II] (red) and the comparison (black) samples respectively. Right panels: observed (hatched pink histogram) and extinction-corrected (hatched gray histogram) L([O II]) luminosities. Vertical dashed lines indicate the median value for the observed (red) and extinction-corrected (black) luminosity distributions.

The stellar mass and the [O II] observed (not corrected for dust extinction) luminosity distributions, $L([O\,II])_{obs}$, for the two samples of SHARDS [O II] emitters at redshifts ∼0.84 and ∼1.23 are shown in Figure 12 (left panels). The average values of the stellar mass in the two redshift bins are similar, passing from $\langle \log(M/M_{\odot}) \rangle \sim 9.3$ at $z \sim 0.84$ to $\langle \log(M/M_{\odot}) \rangle \sim 9.5$ at $z \sim 1.23$ (left panels). We also note that the average stellar mass is very similar to that obtained for the parent samples for the two redshift intervals (overplotted as black histograms).

In the right panels of Figure 12 we show instead the distribution of the observed and extinction-corrected [O II] luminosities ($L([O\,II])_{obs}$ and $L([O\,II])_{cor}$), adopting the extinction values derived from our two-population SED-fitting technique. The average optical extinction values, for the old and young populations, are $A_{old} \sim 0.9$ and $A_{you} \sim 1.5$,

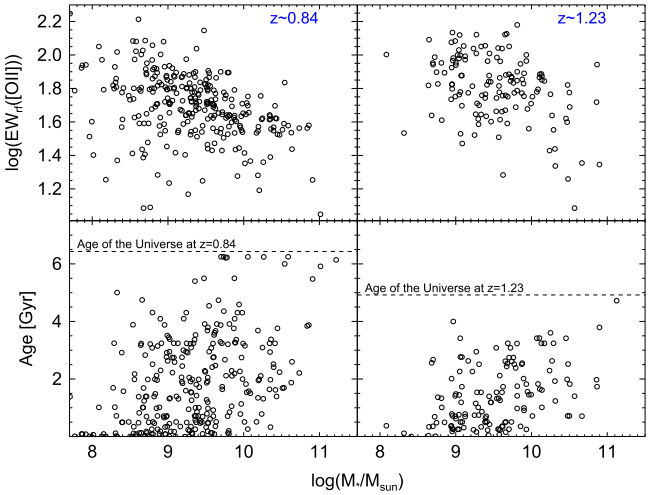

Figure 13. Relations between (mass-weighted) stellar ages, stellar masses, and EW_{rf}([O II]) for the $z = 0.84$ (left panels) and $z = 1.23$ [O II] emitters. These quantities were derived from two-population SED fitting models that assumed a Chabrier IMF, exponentially declining SFHs, and Calzetti et al. (2000) internal dust reddening. See the text for details on the SED modeling.

respectively. We adopt the extinction from the young population to correct the [O II] luminosities, since [O II] emission is expected to be mostly produced in young star-forming regions. An attenuation law of Calzetti et al. (2000) is assumed, with a factor ∼2.3 accounting for the conversion from the stellar to the gas extinction. This conversion factor has been derived for a sample of local SFGs, while recent studies have suggested that it might be evolving with redshift (see, e.g., Wuyts et al. 2011; Kashino et al. 2013; Pannella et al. 2015; Talia et al. 2015). Nonetheless, due to the large uncertainties in the derivation of this factor we preferred to use the classical value for local galaxies.

The median values for $L([\mathrm{O\,II}])_{\mathrm{obs}}$ are $\sim 10^{40.9}$ erg s^{-1} and $\sim 10^{41.2}$ erg s^{-1} for the F687W17 and F823W17 samples respectively, which shift to $\sim 10^{41.2}$ erg s^{-1} and $\sim 10^{41.4}$ erg s^{-1} for $L([\mathrm{O\,II}])_{\mathrm{cor}}$. The median values for the observed and corrected [O II] luminosity distributions increase by about ∼0.2–0.3 dex from the lower to the higher redshift bin.

In Figure 13 we plot the M_*–age and M_*–EW_{rf}([O II]) diagrams for the two samples of [O II]-selected ELGs at $z \sim 0.84$ and ∼1.23. Despite the large scatter and intrinsic uncertainties present in the diagrams, we can draw some conclusion about the relation of [O II] EWs, stellar population ages, and galaxy stellar masses. More specifically, if we divide our samples into subsamples containing galaxies above or below the median value of EW_{rf}([O II]), we see that the median value of the mass is ∼4 (∼2) times larger for galaxies in the low-EW_{rf}([O II]) sample than for galaxies belonging to the high-EW_{rf}([O II]) sample at $z \sim 0.84$ ($z \sim 1.23$).

Regarding the ages of the stellar populations we do not see any specific trend related to the EW of the [O II]-selected galaxies. Instead, we see that galaxies with masses below the median mass value are on average younger, by a factor of ∼2 (∼4), than the more massive galaxies for the $z \sim 0.84$ ($z \sim 1.23$) sample, as might be expected within the *downsizing* scenario of galaxy evolution, where massive galaxies form the bulk of their mass at an early stage of evolution. These results are in qualitative agreement, for example, with those from Ly et al. (2012), although we find larger average stellar ages perhaps because our fitting method includes two populations (and thus is less affected by recent bursts of SF).

Finally, in Figure 14, we plot the SFR–M_* diagram for our [O II] samples. In these plots we correct (assuming for the dust attenuation the prescription detailed below) the SFR derived from the observed $L([\mathrm{O\,II}])_{\mathrm{obs}}$ through the Kewley et al. (2004) relation:

$$\mathrm{SFR}_{\mathrm{obs}}(\mathrm{O\,II}) = (1.4 \pm 0.4) \times 10^{-41} L([\mathrm{O\,II}])\ [M_\odot\ \mathrm{yr}^{-1}] \quad (5)$$

and scale the SFR from Salpeter to Chabrier IMF by dividing by 1.7.

We derive the extinction from the ratio of total SFR to the observed $\mathrm{SFR}_{\mathrm{obs}}$([O II]), where the total SFR is a combination of the obscured and unobscured contributions represented by the UV and IR SFR estimates (or predicted values from best SED fits when dealing with IR non-detections). We adopt here the parameterization introduced by Iglesias-Parámo et al. (2006, see also Bell 2003; Hirashita et al. 2003; Iglesias-Páramo et al. 2004; Moncelsi et al. 2011):

$$\mathrm{SFR} = \mathrm{SFR}_{\mathrm{obs}}(\mathrm{UV}) + (1 - \eta) \times \mathrm{SFR}_{\mathrm{obs}}(\mathrm{IR}) \quad (6)$$

which includes a correction factor $(1 - \eta)$ accounting for the non-negligible contribution to dust heating coming from old stellar populations that would bias the SFR estimate toward higher values. We assume $\eta = 0.32$ and $\eta = 0.09$ depending on the IR luminosity being lower than $10^{11} L_\odot$ and higher than $10^{11} L_\odot$ respectively (see Moncelsi et al. 2011).

The observed SFRs were estimated for all galaxies in the parent sample based on either mid- and far-IR data from *Spitzer* and *Herschel* or on UV luminosities. GOODS-N has been observed with the deepest MIPS data in the sky, with a 5σ limit of 30 μJy (Pérez-González et al. 2005), and also very deep PACS and SPIRE observations, with 5σ limits of 1.7 mJy and 9 mJy at 100 μm and 250 μm, respectively. These limits (the deepest being MIPS 24 μm data) correspond roughly to 5–10 $M_\odot\ \mathrm{yr}^{-1}$ for galaxies at $1.0 < z < 1.5$ (Pérez-González et al. 2005; Elbaz et al. 2011).

The total infrared luminosity, L(IR[8–1000]), has been estimated from SED fitting of the MIR-to-FIR photometry using the templates of Chary & Elbaz (2001), Dale & Helou (2002), and Rieke et al. (2009). The infrared luminosities are then converted into SFRs using the Kennicutt (1998) relation:

$$\mathrm{SFR}_{\mathrm{obs}}(\mathrm{IR}) = 2.7 \times 10^{-44} L(\mathrm{IR})\ \left[M_\odot\ \mathrm{yr}^{-1}\right] \quad (7)$$

normalized to a Chabrier IMF. In order to estimate SFRs for galaxies not detected in the mid-or far-IR (including the quiescent galaxy sample), we used UV luminosities at rest-frame 280 nm. These luminosities were converted into SFRs by applying Kennicutt (1998) equation normalized to a Chabrier IMF:

$$\mathrm{SFR}_{\mathrm{obs}}(\mathrm{UV}) = 0.95 \times 10^{-28} L(\mathrm{UV})\ \left[M_\odot\ \mathrm{yr}^{-1}\right]. \quad (8)$$

The UV-based SFRs were corrected for attenuation following the recipe from Meurer et al. (1999), based on the UV/IR-β relation (IRX-β). The UV slope β for each galaxy was measured from the SEDs, interpolating the best fitting models between 150 and 300 nm.

We compare our results with the SFR–M_* relation from Whitaker et al. (2012), who studied the evolution of the SFR–

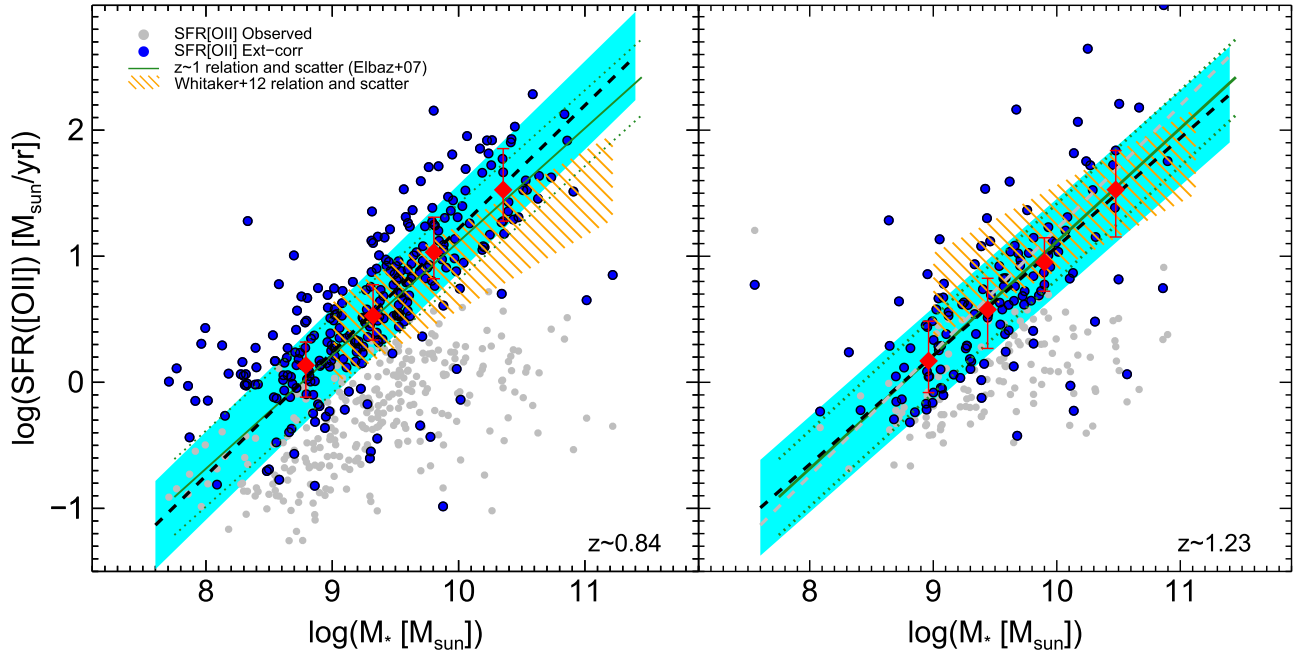

Figure 14. SFR derived from the [O II] line vs. stellar mass relation at redshifts $z \sim 0.84$ (left panel) and $z \sim 1.23$ (right panel). Observed SFR([O II]) (gray filled dots) and extinction-corrected SFR([O II]) (blue open dots) are shown in the plot. The black dashed line is the fit to our data, with the scatter in the relation shown as the cyan shaded area. For comparison, we also overplot, as red diamonds with error bars, the median and (first and third) quartiles for the four equally populated mass bins including 90% of data (i.e., clipping extremes). The orange shaded area indicates the SFR–M_* relation (and its scatter) from Whitaker et al. (2012) for the two redshift bins. The green continuum and dotted lines represent the SFR–M_* at redshift $z \sim 1$ and its 68% confidence interval, respectively, from Elbaz et al. (2007). In the right panel, we also depict as a gray dashed line the SFR–M_* relation from the left panel.

M_* relation up to redshift 2.5 for a sample of >20,000 galaxies from the NEWFIRM Medium-band Survey, shown as the orange hatched region. Comparing the linear fit to our data (dashed black lines in Figure 14) with the SFR–M_* relation at the same redshift from Whitaker et al. (2012), we observe a slightly larger slope in our case. This can be due to the different selections applied in the two cases; in fact a larger slope is also found by Whitaker et al. (2012) when selecting only blue SF galaxies, which might be more comparable with our [O II] selection.

Indeed, we should mention that there could be metallicity effects, in the sense that for higher masses we expect higher metallicities, and then we can have larger L([O II]) for the same SFR. In this sense, our SFR([O II]) could be overestimated at large masses.

As a check, we have also derived SFR([O II]) using the mass-dependent calibration for the dust extinction from Garn & Best (2010). Using this relation, we would recover a better agreement with the results from Whitaker et al. (2012), in terms of slope of the massive end of the SFR–M_* diagram.

On the other hand, we compare our SFR–M_* relation with the one presented by Elbaz et al. (2007) for redshift $z \sim 1$ SF galaxies and find very good agreement between their logarithmic slope of ∼0.9 and our best linear fit that provides a logarithmic slope of ∼0.98 at $z \sim 0.84$ and ∼0.86 at $z \sim 1.23$, and a scatter of ∼0.35 and ∼0.38, respectively, at these two redshifts.

As noted in Whitaker et al. (2012) a flattening of the SFR–M_* relation moving toward higher redshifts has been observed in several previous works (see, e.g., Noeske et al. 2007; Karim et al. 2011) and confirmed using our [O II]-selected sample of SF galaxies using SHARDS data. Nonetheless, as also commented in Section 1, various effects can contribute to bias these results, leading to a flattening of the SFR–M_* relation, especially for the higher redshift samples, where the mass completeness may represent a major issue.

5. COMPARISON OF SFGs AND QUIESCENT GALAXY SELECTIONS

In this section, we compare the SF properties (as derived from SED fitting) of the [O II]-selected samples with the complementary samples introduced in Section 2.4 (nominally, the mass-selected, the IR-detected, and the quiescent *UVJ*-selected samples). This allows us to investigate the effect of different sample selections on the determination of the main sequence for SFGs and to highlight the possible biases introduced by each selection.

As recently discussed in various works (see, e.g., Rodighiero et al. 2014; Speagle et al. 2014), the determination of the SFR–M_* relation using various sample definitions, related to different SFR indicators, can lead to different determinations for the slope of this fundamental observed relation, with a steeper relation typically found when using UV-selected galaxies than, e.g., the IR-detected galaxy samples. This is also partially attributed to possible Malmquist bias introduced when using IR-selected galaxies, more easily detected at increasing masses.

Nonetheless, as shown in Figure 15, this dependence of the slope on the sample selection is not clear in our samples at redshift $z \sim 1$. In fact, we find very similar logarithmic slopes (in all cases ∼1) for the SFR–M_* relation of the general parent sample and the different subsamples selected on the basis of their IR and [O II] emission (represented by the black, magenta, and blue dashed lines in Figure 15). For completeness, we also plot the best-fit linear relation for the subsample of quiescent

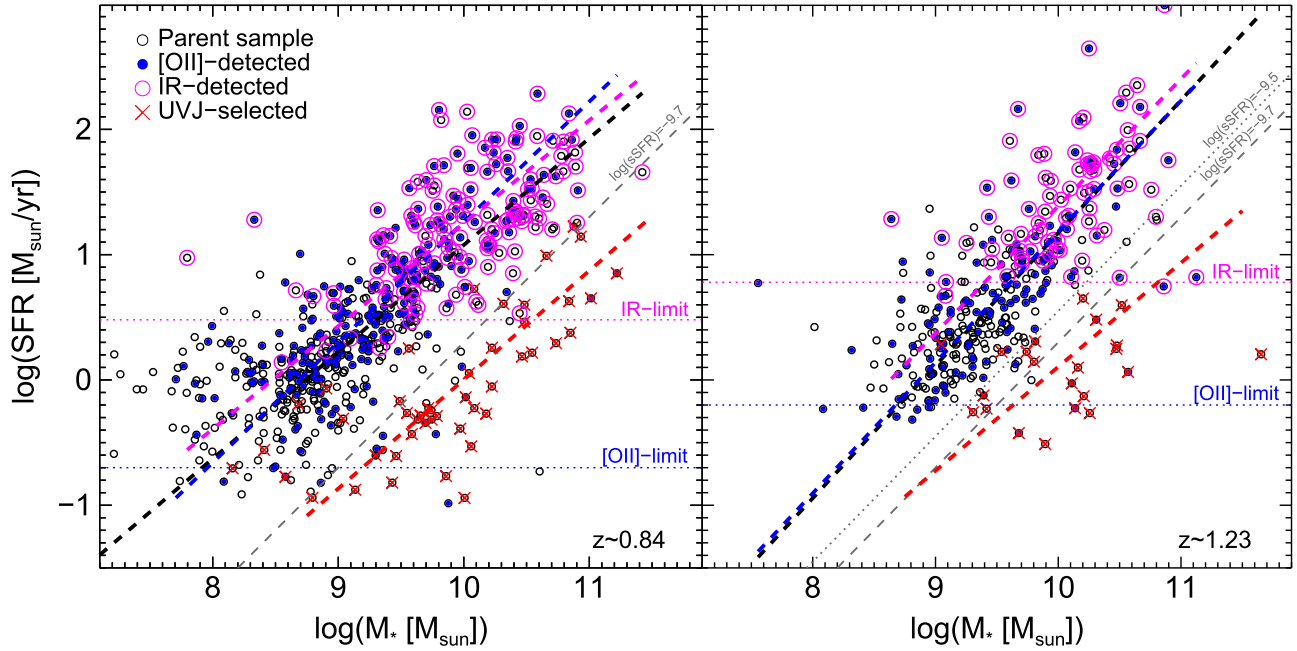

Figure 15. Star formation rate vs. stellar mass diagrams (as derived from SED fitting) for the different sample selections indicated in the legend. The dashed lines, identified by the color corresponding to the symbols in the legend, represent the linear fits to the SFR–M_* relation for each subsample. The dark-gray dashed and dotted lines give the the SFR–M_* for galaxies with a constant log(sSFR [yr^{-1}]) = −9.7 or −9.5 respectively. See the text for details.

(*UVJ*-selected) galaxies, which lies well below the main sequence for SF galaxies.

The total and normalized distributions of M_*, SFRs, and sSFRs for each subsample are given in Figure 16. We observe that, at $z = 0.84$, the [O II] emitters have a very similar stellar mass distribution to the parent sample, maybe with a deficit at low masses (as can be seen from the normalized histograms in Figure 16). However, many galaxies (aproximately 50%) below log(SFR [$M_\odot\,\mathrm{yr}^{-1}$]) = 0.8, i.e., 5–6 $M_\odot\,\mathrm{yr}^{-1}$ are not [O II] emitters or are not detected by our survey. Since the expected SFR detection limit, derived from the 3σ flux detection limit for our survey in each filter (blue dotted lines in the central panels of Figure 10), is log(SFR [$M_\odot\,\mathrm{yr}^{-1}$]) ∼ (−0.2)–(−0.7), i.e., ∼0.6–0.2 $M_\odot\,\mathrm{yr}^{-1}$, we conclude that this fraction of undetected low-SF galaxies are not due to a detection threshold but have their [O II] emission prevented/quenched by some physical mechanism, e.g., low excitation due to the weak SF activity. In the case of IR emitters, it is clear that they concentrate at the high-mass end of the population, and probably the detection limit—of ∼5 $M_\odot\,\mathrm{yr}^{-1}$ (shown magenta dotted in Figure 16)—precludes the detection of low-SF galaxies. A similar result is seen at $z = 1.23$.

The distributions of sSFR for the different samples are given in the right panels of Figure 16. Interestingly, there is good agreement between the global sSFR distribution of the parent, [O II]-selected, and IR-selected samples of galaxies. This similarity of the sSFR distributions is mirrored by the presence of very similar main sequences for the various samples (see Figure 15) with a quite constant slope. Other recent studies have argued the presence of a knee in the SFR–M_* relation, but we do not see it in our samples (see, e.g., Whitaker et al. 2014; Kochiashvili et al. 2015; Lee et al. 2015). As expected, the *UVJ*-selected sample of quiescent galaxies exhibits a distribution of sSFR with very small values with respect to the other sample selections.

Observing the normalized distributions, shown in the lower panels of each row of plots in Figure 16, we can conclude that there is no (or only mild) mass-selection bias in the case of [O II] emitters, while the IR-detected and *UVJ*-selected samples are systematically shifted toward higher masses. The peak in the SFR distribution is only slightly enhanced for the [O II] sample, with respect to the parent sample, whereas the peaks for the IR-detected and *UVJ*-selected samples are clearly shifted toward higher and lower SFRs, respectively. Similar conclusions apply to both redshift ranges.

As already discussed in Section 2.4, the assumed sSFR cut at log(sSFR [yr^{-1}]) = −9.7 (shown as dark-gray dashed lines in Figure 15) leads to a good overlap between the *UVJ* selection criteria and a pure sSFR selection for the lower redshift sample, while a slightly higher sSFR cut (log(sSFR [yr^{-1}]) = −9.5, shown as a dark-gray dotted line in the right panel of Figure 15) would better reconcile the two definitions (i.e., *UVJ*-selected and sSFR-based) of *quiescent galaxies* for the higher redshift sample. This difference might be related to a small evolution of the SF properties between these two redshift intervals (corresponding to ∼1.5 Gyr in time).

Indeed we remark that a relatively large fraction of galaxies selected as quiescent using these two alternative definitions are detected as [O II] or IR emitters. In fact we find ∼20% and ∼25% of the lower redshift galaxy sample to have an [O II] or IR detection, for the *UVJ*- and sSFR-selected samples, respectively. These fractions increase to ∼30% and ∼40% for the higher redshift sample. These results show, on the one hand, that the *UVJ*-selection seems to be more effective in the selection of bona fide quiescent galaxies than a simple cut in the sSFR, and on the other that the contamination from SF galaxies starts to be very relevant when moving to higher redshifts. This result is in agreement with recent results on the study of quiescent galaxies selected in the *UVJ* plane (see, e.g., Belli et al. 2015).

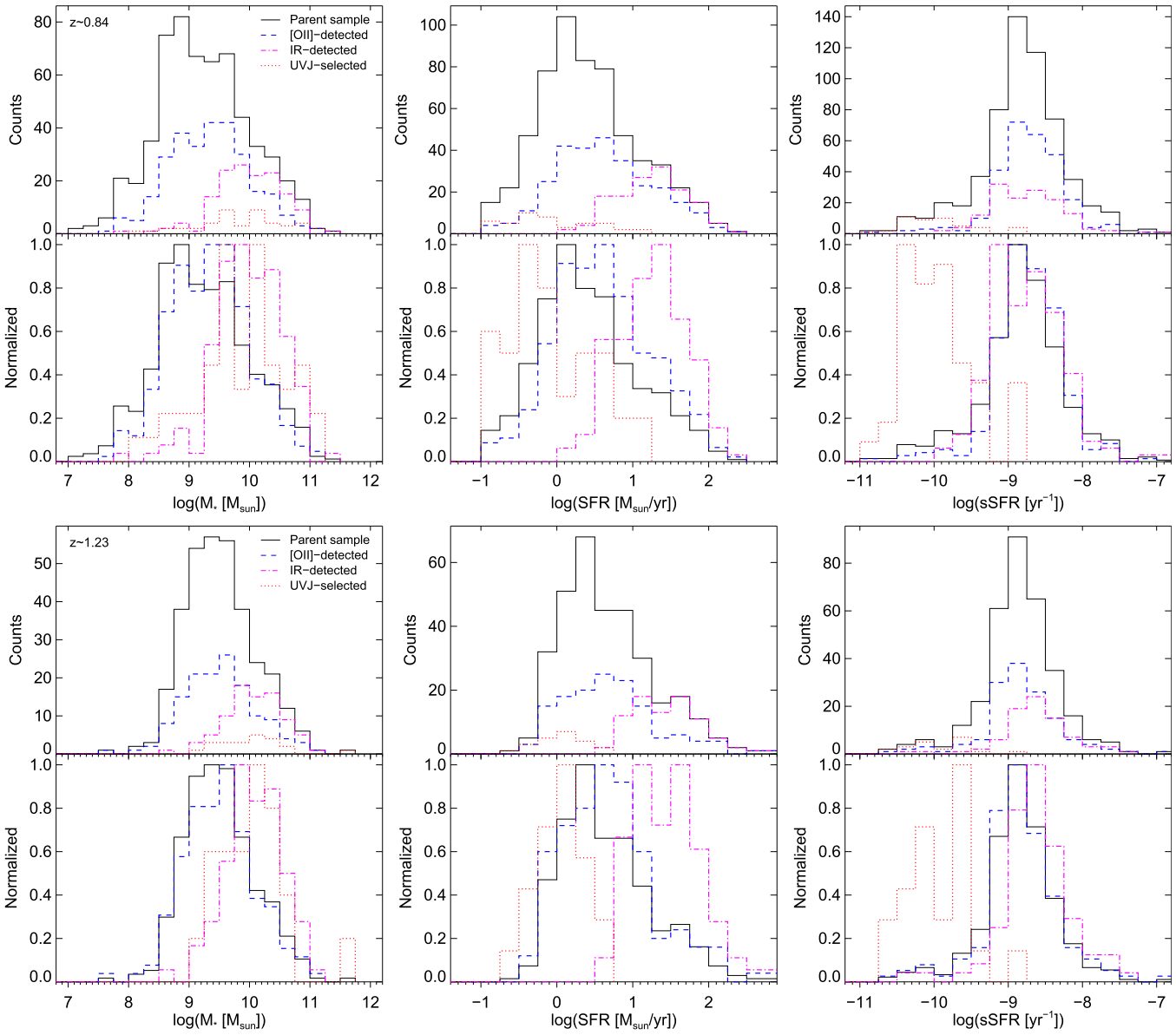

Figure 16. Distribution of M_*, SFR, and sSFR for the $z \sim 0.84$ (top panels) and $z \sim 1.23$ (bottom panels) samples. Upper panels in each plot represent the general number distributions and lower panels give the histograms normalized to the peak, for each sample indicated in the legend (reported only in the stellar mass plots).

6. DUST ATTENUATION PROPERTIES

Previous studies have found that the dust attenuation is a strong function of stellar mass (e.g., Reddy et al. 2006, 2010; Pannella et al. 2009; Wuyts et al. 2011; Whitaker et al. 2012), where the most massive galaxies are more highly obscured.

We parameterize the attenuation as the ratio of the total SFR (see Section 4 for the detailed definition) to the observed SFR_{obs} for each SF indicator (UV1600, UV2800, [O II], and IR). We find a similar trend using the SHARDS samples of [O II]-selected galaxies in Figure 17: more massive galaxies have larger SFR/SFR_{obs} ratios. We depict as solid symbols IR-detected galaxies for which the determination of the total SFR is more reliable, while arrows represent galaxies selected on the basis of their [O II] emission but lacking IR detection, which may lead to an underestimation of the total SFR. Indeed, by selecting [O II] ELGs we are possibly biasing the estimated average attenuation toward lower values, since galaxies suffering strong dust attenuation should have their [O II] emission reduced or undetectable.

The IR alone is a good estimator of the total SFR for most galaxies, but a fraction of them have non-negligible amounts of dust-free SF, and that seems to be more significant for lower masses. There are approximately 20% (25%) of galaxies detected in the IR for which the contribution to the total SFR from unobscured SF is larger than 30% at redshift ∼0.84 (∼1.23), most of them being less massive than 10^{10} $M_\odot$, and with total SFR lower than 20 $M_\odot$ yr^{-1}.

An analogous behavior for the attenuation is found with respect to the total SFR (right panels in Figure 17), where the trend appears even more evident and the relation tighter with a smaller scatter. Galaxies sustaining higher SFRs also exhibit larger dust attenuation (consistently with earlier results for SFGs, e.g., Domínguez Sánchez et al. 2012, 2014). This characteristic may be related to the fact that more actively star-forming galaxies possibly hold higher fractions of dust

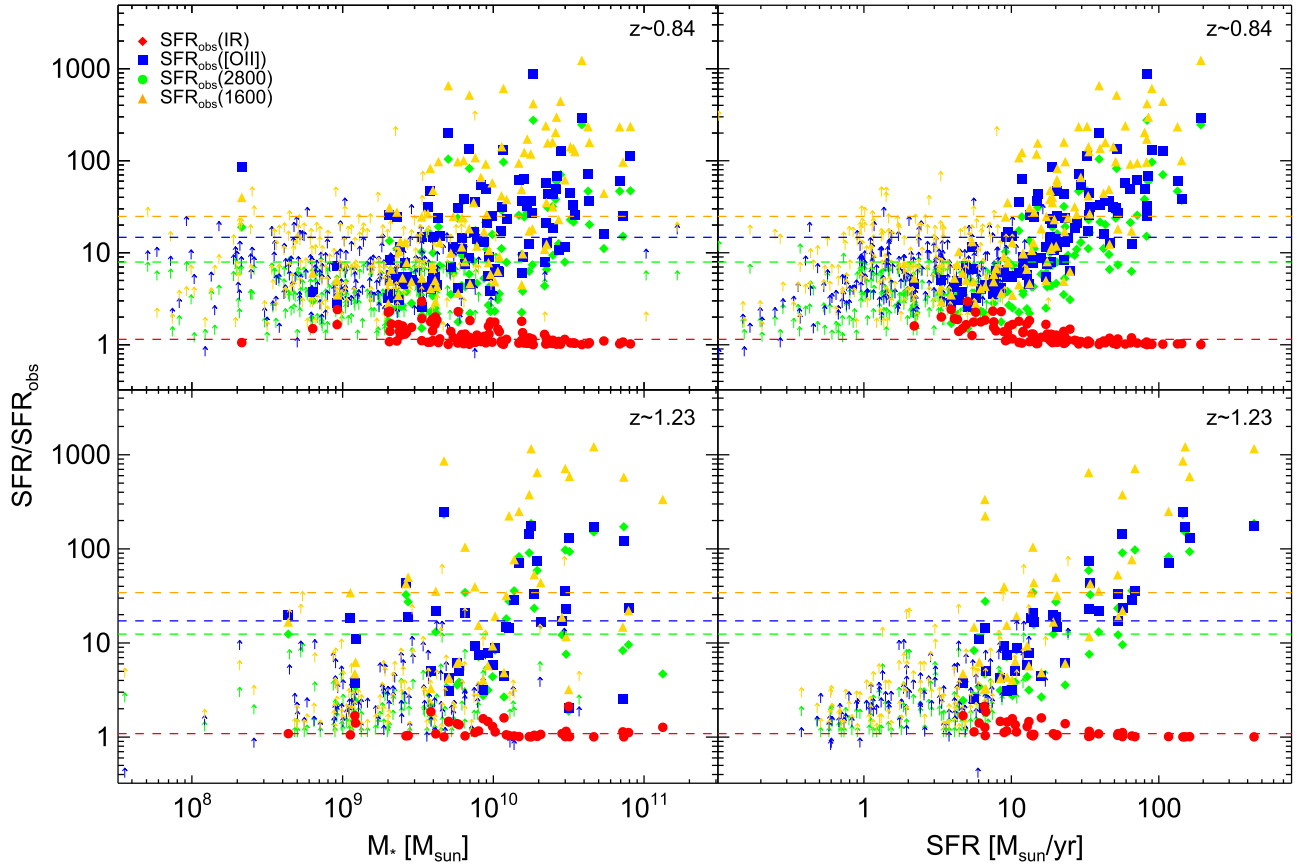

Figure 17. Top panels: ratio between the total SFR and the observed SFR_{obs} for UV(1600), UV(2800), [O II], and IR SFR indicators vs. the stellar mass (left panel) and the total SFR (right panel) at redshift ∼0.84 (F687W17). Arrows represent lower limits for the galaxies not detected in the IR. Dashed lines represent the median values computed for IR-detected galaxies only. Bottom panels: the same for galaxies at redshift ∼1.23 (F823W17).

sustaining this high rate of SF or it could be ascribed to a higher efficiency in heating the dust in these galaxies. The median value of the ratio SFR/SFR_{obs}, where SFR_{obs} is estimated from the UV(1600), UV(2800), [O II], or IR observed (i.e., not extinction-corrected) SFR respectively, is found to increase smoothly as the wavelength of the SFR indicator decreases.

Interestingly, the trend of the M_*–SFR/SFR_{obs} relation in the two redshift bins considered does not seem to vary significantly, suggesting no (or weak) evolution of the dust attenuation properties between these two epochs (separated by ∼1.5 Gyr in time). Indeed, the attenuations of the line and continuum photons as represented by the [O II] and UV(2800) SF indicators are quite similar, again suggesting that [O II] can be considered a reliable SF indicator.

The results presented in Figure 17 also suggest that galaxies of different masses are dominated by different mechanisms of SF. The SFR is mostly dominated by the IR emission, when this is detectable, especially for more massive galaxies. This is indicated also by the tightening of the SFR/SFR_{IR} around 1 for high masses. Massive galaxies may present violent and explosive processes of SF (traced by high dust fractions), while less massive galaxies would undergo more relaxed episodes of SF. We can interpret these results as indicative of highly unstable SF processes dominating in the massive galaxies, e.g., driven by galaxy interactions/mergers or violent relaxation in highly unstable (clumpy) disks. Less massive galaxies would instead be characterized by a more diffuse SF. The investigation of the relation between morphology/environment and SF properties is beyond the scope of this paper and is deferred to a dedicated work.

7. SUMMARY AND CONCLUSIONS

We have presented a detailed analysis of a complete sample of SFGs at $z \sim 0.84$ and $z \sim 1.23$. The sample is a comprehensive compilation of sources selected with three different SFR tracers: the [O II] emission line, the UV emission, and the MIR/FIR emission. Concerning [O II] emitters, we have selected them down to very faint magnitudes (∼26.5 mag), benefitting from the ultra-deep spectro-photometric data from the SHARDS survey (see Pérez-González et al. 2013). The sample of [O II] emitters has been compared with the general population of stellar mass-selected galaxies (including from quiescent to starburst galaxies) at the mentioned redshifts. The SF activity and extinction properties of the whole population of galaxies at $z \sim 0.84$ and $z \sim 1.23$ have been characterized with specific SFR estimations, as well as *UVJ* colors and dust emission measurements based on *Spitzer* and *Herschel* data.

The SHARDS data, combined with a customized and refined method for selection of ELGs using its medium-band (∼150 Å) filters and for determination of the continuum on the basis of SED fitting, are suitable for ELG studies and have allowed us to obtain the results summarized below.

1. We have developed a technique that optimally exploits the medium-band characteristics of the ultra-deep SHARDS survey to perform for the first time a systematic and robust detection of emission lines in low-, intermediate-, and high-redshift galaxies, inspired by the traditional procedures based on narrow-band imaging.
2. We have demonstrated that the depth and image quality of our survey allow us to recover virtually all ELGs that have already been confirmed by the deepest spectroscopic surveys carried out in the GOODS-N field. We have shown that we are able to extend these spectroscopic studies of ELGs, typically limited to $R \sim 24$–25 mag, to fainter magnitudes ($R \sim 26$–27 mag) and detect strong [O II] emitters with faint continuum emission (i.e., large EWs), as well as Lyα emitters up to $z \sim 6$ (Rodríguez Espinosa et al. 2014).
3. By combining all the SHARDS filter data and fitting them to stellar population synthesis models, we have shown that we can robustly measure EWs and fluxes for these emission lines down to $EW_{rf}([O\,II]) \sim 15$–20 Å and $F([O\,II]) \sim (2$–$3) \times 10^{-18}$ erg s^{-1} cm^{-2} respectively. These values are very similar to what can be done with deep spectroscopy. But spectroscopic surveys typically preselect their targets based on broad-band magnitudes ($R < 24$–25 mag) and have limited completeness because they can only put a limited number of slits in every object, unless a huge amount of observing time is granted. By using our medium-band selection technique, we get all emitters without any strong selection effect and down to fainter broad-band magnitudes.
4. We have focused this paper on two redshift ranges: one based on the selection of galaxies with emission lines lying within the F687W17 filter (central wavelength: 687 nm) and another sample selected with the F823W17 filter. For [O II] emitters, these wavelengths correspond to $z \sim 0.84$ and $z \sim 1.23$. The use of the SHARDS-based photometric redshifts allowed us to extend (by a factor $\sim$3 in numbers) the samples selected based only on confirmation of spectroscopic redshift available from the literature. We can robustly measure [O II] fluxes and EWs even for galaxies that typically do not have sufficiently high-quality spectra for measurements of this kind (including galaxies usually exhibiting [O II] emission but lacking continuum detection).
5. The full SHARDS data set, spanning the optical range from 500 to 950 nm, has allowed a significant improvement (about one order of magnitude, reaching $\sigma_{zphot} \lesssim 0.5\%$ at redshift $z \sim 1$) on the photometric redshift accuracy (see Pérez-González et al. 2013; Ferreras et al. 2014; G. Barro et al. 2015, in preparation) with respect to the use of previously available broad-band data. The accuracy in the photo-z determination is mirrored in the high success rate ($\gtrsim$90%–95%) and low contamination levels ($\lesssim$5%–10%) of the selected samples of [O II] emitters.
6. We have analyzed the $EW_{rf}([O\,II])$ distribution for the two samples of [O II] emitters, finding robust evidence for the evolution of the average $EW_{rf}([O\,II])$ with cosmic time at least up to redshift $\sim$1, followed by a possible flattening, in good agreement with what is found by studying the SFRD evolution of the universe. Thus, globally speaking, the [O II] emission is a good tracer of the SFR evolution, despite the complicated dependence on intrinsic physical parameters such as metallicity and temperature, among others.
7. We have found that galaxies with low-$EW_{rf}([O\,II])$ (i.e., below the median $EW_{rf}([O\,II])$) have on average higher masses than galaxies with high-$EW_{rf}([O\,II])$ (by a factor $\sim$4 and $\sim$2 for the samples at $z \sim 0.84$ and $z \sim 1.23$, respectively). We do not see a similar trend with respect to the age of the stellar populations. Instead, we observe that galaxies with masses below the median value are on average younger, by a factor of $\sim$2 ($\sim$4), than the more massive galaxies for the $z \sim 0.84$ ($z \sim 1.23$) sample. As might be expected from the downsizing scenario, massive galaxies seem to have formed the bulk of their stellar mass at an earlier epoch.
8. We derive the SFR([O II]) and compare the SFR–M_* relation for our samples with previous results from the literature. We find a steeper slope ($\alpha \sim 0.9$) of the relation for both redshift intervals than Whitaker et al. (2012), but this is compatible with their results when selecting blue galaxies (or in the case where we adopt a mass-dependent extinction calibration). Additionally, our data suggest a trend of the slope with redshift, with higher redshift galaxies showing shallower slopes (despite the various caveats related to possible observational biases). Indeed the slope of the SFR–M_* relation for our [O II] emitters is in very good agreement with the main sequence of $z \sim 1$ SF galaxies defined in Elbaz et al. (2007). Also the scatter in the relation ($\sim$0.35–0.38 dex) is in agreement with previous determinations.
9. We have compared the distributions of physical properties and the SFR–M_* relation for the [O II]- and IR-detected samples with those of the general population of galaxies at the same redshift (parent sample), finding no evident bias introduced on the SFR–M_* relation by any of the selections of SFGs. Quiescent galaxies (identified on the basis of the *UVJ* diagram or a sSFR cut) populate a separated locus in the SFR–M_* diagram and follow an independent relation, although there is a large scatter in the data points and some outliers with higher SFRs.
10. We have discussed the possible biases affecting the different samples, comparing the total and normalized distributions for the M_*, SFRs, and sSFRs, for the subsamples of [O II]-selected, IR-detected, and *UVJ*-selected quiescent galaxies, in the two selected redshift bins. We find only a very mild trend in selecting more massive galaxies based on the detection of the [O II] emission line. A stronger bias is found relative to the M_* and SFR distributions of IR-detected galaxies and (as expected) for the quiescent sample. We ascribe the larger bias for the IR-detected samples of galaxies to their larger limits for mass and SFR detection.
11. We observe very similar sSFR distributions for the parent sample and the [O II]- and IR-detected samples of SF galaxies. This behavior is related to the very similar SFR–M_* relations found for the various samples. We do not observe significant variations in the slope of the main sequence of SF galaxies at high masses ($M_* > 10^{10}\,M_\odot$), as claimed by other recent works.
12. We observe that the sample of quiescent galaxies, independently from the definition based on a *UVJ* diagram or a sSFR cut, can be contaminated by both

[O II]- and IR-detected galaxies. We find that ∼20% and ∼25% of the lower redshift galaxy sample present [O II] or IR detection, for the *UVJ*- and sSFR-selected samples respectively. These fractions increase to ∼30% and ∼40% for the higher redshift sample. We deduce that the *UVJ* selection seems to be more effective in the selection of bona fide quiescent galaxies than a simple cut in the sSFR; on the other hand we note that on moving to higher redshifts the contamination from SF galaxies starts to be very relevant and that more careful (redshift-dependent) selection criteria should be adopted.

13. We observe that the IR emission alone is a good estimator of the total SFR for most galaxies, but a fraction of them have non-negligible amounts of dust-free SF, and that seems to be more significant for lower masses. Approximately 20% (25%) of IR-detected galaxies present a contribution to the total SFR from unobscured SF larger than 30% at redshift ∼0.84 (∼1.23), most of them being less massive than 10^{10} $M_{\odot}$ and with total SFR lower than 20 $M_{\odot}$ yr^{-1}.
14. We have finally found that the dust attenuation (as indicated by the ratio of the total to the observed SFR for each SFR indicator) strongly correlates with the stellar mass and total SFR of the galaxies. This result might be related to a higher dust content for more massive galaxies or to a higher dust heating efficiency in these massive objects. The dust attenuation correlates linearly with stellar mass, and the trend of the stellar mass–dust attenuation relation does not show significant differences between the two redshift ranges, suggesting no (or slow) evolution of dust attenuation properties between these two epochs (∼1.5 Gyr apart). These results also suggest that galaxies of different masses are dominated by different mechanism of SF, with massive galaxies exhibiting more violent and explosive processes of SF (traced by the higher dust fractions), while less massive galaxies would undergo more moderate episodes of SF.

We have shown the huge potential of SHARDS ultra-deep data in studying galaxy evolution using ELGs. We plan to extend the results presented in this work using the whole SHARDS data set (including 25 filters and several detected lines) to constrain the evolution of the physical properties of SFGs in the redshift interval $0.3 < z < 2$, fully covering the epoch where strong evolutionary processes shaped the galaxy populations toward the present-day universe.

The authors would like to thank the referee for her/his valuable comments and helpful suggestions concerning the presentation of this paper, which helped to improve the manuscript. The work of A.C. is supported by the STARFORM Sinergia Project funded by the Swiss National Science Foundation, and also benefited from a MERAC Funding and Travel Award. A.C. acknowledges the kind hospitality of the Departamento de Astrofísica y ciencias de la Atmósfera, Universidad Complutense de Madrid, and of the Department d'Astronomia i Astrofisica, Universitat de Valencia. A.C. and E.R. are grateful to M. Cava for many useful discussions and suggestions. E.R. acknowledges the kind hospitality of the Observatoire de Genève, Université de Genève. P.G.P.-G. acknowledges support from the Spanish Programa Nacional de Astronomía y Astrofísica under grants AYA2012-31277. A.V.G. acknowledges support from the ERC via an Advanced Grant under grant agreement no. 321323-NEOGAL. N.C. acknowledges support from the Spanish Ministry of Economy and Competitiveness under grant AYA2013-46724-P. A.A.H. and A.H.C. acknowledge financial support from the Spanish Ministry of Economy and Competitiveness through grant AYA2012-31447, which is partly funded by the FEDER program. A.J.C. is a Ramón y Cajal Fellow of the Spanish Ministry of Science and Innovation and acknowledges financial support from the Spanish Ministry of Economy and Competitiveness through grant AYA2012-30789, partly funded by the FEDER program. This work has made use of the Rainbow Cosmological Surveys Database, which is operated by the Universidad Complutense de Madrid (UCM). Based on observations made with the Gran Telescopio Canarias (GTC), installed at the Spanish Observatorio del Roque de los Muchachos of the Instituto de Astrofísica de Canarias, on the island of La Palma.

REFERENCES

Adams, J. J., Blanc, G. A., Hill, G. J., et al. 2011, ApJS, 192, 5
Alexander, D. M., Bauer, F. E., Brandt, W. N., et al. 2003, AJ, 126, 539
Baldry, I. K., & Glazebrook, K. 2003, ApJ, 593, 258
Balogh, M. L., Morris, S. L., Yee, H. K. C., Carlberg, R. G., & Ellingson, E. 1999, ApJ, 527, 54
Barger, A. J., Cowie, L. L., & Wang, W.-H. 2008, ApJ, 689, 687
Barro, G., Pérez-González, P. G., Gallego, J., et al. 2011a, ApJS, 193, 13
Barro, G., Pérez-González, P. G., Gallego, J., et al. 2011b, ApJS, 193, 30
Bell, E. F. 2003, ApJ, 586, 794
Bell, E. F., Papovich, C., Wolf, C., et al. 2005, ApJ, 625, 23
Belli, S., Newman, A. B., & Ellis, R. S. 2015, ApJ, 799, 206
Bertin, E., & Arnouts, S. 1996, A&AS, 117, 393
Blanton, M., & Lin, H. 2000, ApJL, 543, L125
Brinchmann, J., Charlot, S., White, S. D. M., et al. 2004, MNRAS, 351, 1151
Bruzual, G. 1983, ApJ, 273, 105
Bruzual, G., & Charlot, S. 2003, MNRAS, 344, 1000
Calzetti, D., Armus, L., Bohlin, R. C., et al. 2000, ApJ, 533, 682
Chabrier, G. 2003, PASP, 115, 763
Chary, R., & Elbaz, D. 2001, ApJ, 556, 562
Ciardullo, R., Gronwall, C., Adams, J. J., et al. 2013, ApJ, 769, 83
Cimatti, A., Cassata, P., Pozzetti, L., et al. 2008, A&A, 482, 21
Cooper, M. C., Aird, J. A., Coil, A. L., et al. 2011, ApJS, 193, 14
Cowie, L. L., Barger, A. J., Hu, E. M., Capak, P., & Songaila, A. 2004, AJ, 127, 3137
Cucciati, O., Tresse, L., Ilbert, O., et al. 2012, A&A, 539, A31
Daddi, E., Renzini, A., Pirzkal, N., et al. 2005, ApJ, 626, 680
Dale, D. A., & Helou, G. 2002, ApJ, 576, 159
Darvish, B., Sobral, D., Mobasher, B., et al. 2014, ApJ, 796, 51
Díaz-García, L. A., Cenarro, A. J., López-Sanjuan, C., et al. 2015, A&A, 582, A14
Domínguez Sánchez, H., Bongiovanni, A., Lara-López, M. A., et al. 2014, MNRAS, 441, 2
Domínguez Sánchez, H., Mignoli, M., Pozzi, F., et al. 2012, MNRAS, 426, 330
Eddington, A. S. 1927, MNRAS, 88, 134
Elbaz, D., Daddi, E., Le Borgne, D., et al. 2007, A&A, 468, 33
Elbaz, D., Dickinson, M., Hwang, H. S., et al. 2011, A&A, 533, A119
Ferreras, I., Trujillo, I., Mármol-Queraltó, E., et al. 2014, MNRAS, 444, 906
Fiore, F., Puccetti, S., Brusa, M., et al. 2009, ApJ, 693, 447
Fiore, F., Puccetti, S., & Mathur, S. 2012, AdAst, 2012, 271502
Frayer, D. T., Huynh, M. T., Chary, R., et al. 2006, ApJL, 647, L9
Gallagher, J. S., Hunter, D. A., & Bushouse, H. 1989, AJ, 97, 700
Gallego, J., Zamorano, J., Aragon-Salamanca, A., & Rego, M. 1995, ApJL, 455, L1
Garn, T., & Best, P. N. 2010, MNRAS, 409, 421
Giavalisco, M., Ferguson, H. C., Koekemoer, A. M., et al. 2004, ApJL, 600, L93
Gilbank, D. G., Baldry, I. K., Balogh, M. L., Glazebrook, K., & Bower, R. G. 2010, MNRAS, 405, 2594
Gilbank, D. G., Bower, R. G., Glazebrook, K., et al. 2011, MNRAS, 414, 304
Hayashi, M., Sobral, D., Best, P. N., Smail, I., & Kodama, T. 2013, MNRAS, 430, 1042

Hernán-Caballero, A., Alonso-Herrero, A., Pérez-González, P. G., et al. 2013, MNRAS, 434, 2136
Hernán-Caballero, A., Alonso-Herrero, A., Pérez-González, P. G., et al. 2014, MNRAS, 443, 3538
Hill, G. J., Gebhardt, K., Komatsu, E., et al. 2008, ASP Conf. Ser. 399, Panoramic Views of Galaxy Formation and Evolution (San Francisco, CA: ASP), 115
Hirashita, H., Buat, V., & Inoue, A. K. 2003, A&A, 410, 83
Hogg, D. W., Cohen, J. G., Blandford, R., & Pahre, M. A. 1998, ApJ, 504, 622
Iglesias-Páramo, J., Buat, V., Donas, J., Boselli, A., & Milliard, B. 2004, A&A, 419, 109
Iglesias-Páramo, J., Buat, V., Takeuchi, T. T., et al. 2006, ApJS, 164, 38
Ilbert, O., Arnouts, S., Le Floc'h, E., et al. 2015, A&A, 579, A2
Jansen, R. A., Franx, M., & Fabricant, D. 2001, ApJ, 551, 825
Karim, A., Schinnerer, E., Martínez-Sansigre, A., et al. 2011, ApJ, 730, 61
Kashino, D., Silverman, J. D., Rodighiero, G., et al. 2013, ApJL, 777, L8
Kauffmann, G., Heckman, T. M., White, S. D. M., et al. 2003, MNRAS, 341, 33
Kelson, D. D. 2014, arXiv:1406.5191
Kennicutt, R. C., Jr. 1998, ARA&A, 36, 189
Kewley, L. J., Geller, M. J., & Jansen, R. A. 2004, AJ, 127, 2002
Kochiashvili, I., Møller, P., Milvang-Jensen, B., et al. 2015, A&A, 580, A42
Kornei, K. A., Shapley, A. E., Martin, C. L., et al. 2012, ApJ, 758, 135
Koyama, Y., Smail, I., Kurk, J., et al. 2013, MNRAS, 434, 423
Kriek, M., Shapley, A. E., Reddy, N. A., et al. 2015, ApJS, 218, 15
Kriek, M., van Dokkum, P. G., Whitaker, K. E., et al. 2011, ApJ, 743, 168
Kron, R. G. 1980, ApJS, 43, 305
Kümmel, M., Walsh, J. R., Pirzkal, N., Kuntschner, H., & Pasquali, A. 2009, PASP, 121, 59
Lee, J. C., Ly, C., Spitler, L., et al. 2012, PASP, 124, 782
Lee, N., Sanders, D. B., Casey, C. M., et al. 2015, ApJ, 801, 80
Le Fèvre, O., Vettolani, G., Garilli, B., et al. 2005, A&A, 439, 845
Lehmer, B. D., Alexander, D. M., Bauer, F. E., et al. 2010, ApJ, 724, 559
Lilly, S. J., Le Fevre, O., Hammer, F., & Crampton, D. 1996, ApJL, 460, L1
Lutz, D., Poglitsch, A., Altieri, B., et al. 2011, A&A, 532, A90
Ly, C., Lee, J. C., Dale, D. A., et al. 2011, ApJ, 726, 109
Ly, C., Malkan, M. A., Kashikawa, N., et al. 2012, ApJ, 757, 63
Madau, P., & Dickinson, M. 2014, ARA&A, 52, 415
Matthee, J. J. A., Sobral, D., Swinbank, A. M., et al. 2014, MNRAS, 440, 2375
McCarthy, P. J., Le Borgne, D., Crampton, D., et al. 2004, ApJL, 614, L9
Meurer, G. R., Heckman, T. M., & Calzetti, D. 1999, ApJ, 521, 64
Moncelsi, L., Ade, P. A. R., Chapin, E. L., et al. 2011, ApJ, 727, 83
Moustakas, J., & Kennicutt, R. C., Jr. 2006, ApJS, 164, 81
Noeske, K. G., Weiner, B. J., Faber, S. M., et al. 2007, ApJL, 660, L43
Oliver, S. J., Wang, L., Smith, A. J., et al. 2010, A&A, 518, L21
Ouchi, M., Shimasaku, K., Akiyama, M., et al. 2008, ApJS, 176, 301
Pannella, M., Carilli, C. L., Daddi, E., et al. 2009, ApJL, 698, L116
Pannella, M., Elbaz, D., Daddi, E., et al. 2015, ApJ, 807, 141
Pereira-Santaella, M., Alonso-Herrero, A., Santos-Lleo, M., et al. 2011, A&A, 535, A93
Pérez-González, P. G., Cava, A., Barro, G., et al. 2013, ApJ, 762, 46
Pérez-González, P. G., Rieke, G. H., Egami, E., et al. 2005, ApJ, 630, 82
Pérez-González, P. G., Rieke, G. H., Villar, V., et al. 2008, ApJ, 675, 234
Pérez-González, P. G., Zamorano, J., Gallego, J., Aragón-Salamanca, A., & Gil de Paz, A. 2003, ApJ, 591, 827
Persic, M., Cappi, M., Rephaeli, Y., et al. 2004, A&A, 427, 35
Pirzkal, N., Burgasser, A. J., Malhotra, S., et al. 2009, ApJ, 695, 1591
Pirzkal, N., Xu, C., Malhotra, S., et al. 2004, ApJS, 154, 501
Reddy, N. A., Erb, D. K., Pettini, M., Steidel, C. C., & Shapley, A. E. 2010, ApJ, 712, 1070
Reddy, N. A., Erb, D. K., Steidel, C. C., et al. 2005, ApJ, 633, 748
Reddy, N. A., Steidel, C. C., Erb, D. K., Shapley, A. E., & Pettini, M. 2006, ApJ, 653, 1004
Ricciardelli, E., Cava, A., Varela, J., & Quilis, V. 2014, MNRAS, 445, 4045
Rieke, G. H., Alonso-Herrero, A., Weiner, B. J., et al. 2009, ApJ, 692, 556
Rodighiero, G., Renzini, A., Daddi, E., et al. 2014, MNRAS, 443, 19
Rodríguez Espinosa, J. M., González-Martín, O., Castro Rodríguez, N., et al. 2014, MNRAS, 444, L68
Salmon, B., Papovich, C., Finkelstein, S. L., et al. 2015, ApJ, 799, 183
Saracco, P., Longhetti, M., Severgnini, P., et al. 2005, MNRAS, 357, L40
Schreiber, C., Pannella, M., Elbaz, D., et al. 2015, A&A, 575, A74
Shivaei, I., Reddy, N. A., Shapley, A. E., et al. 2015a, arXiv:1507.03017
Shivaei, I., Reddy, N. A., Steidel, C. C., & Shapley, A. E. 2015b, ApJ, 804, 149
Sobral, D., Best, P. N., Geach, J. E., et al. 2009a, MNRAS, 398, L68
Sobral, D., Best, P. N., Geach, J. E., et al. 2009b, MNRAS, 398, 75
Sobral, D., Best, P. N., Geach, J. E., et al. 2010, MNRAS, 404, 1551
Sobral, D., Best, P. N., Matsuda, Y., et al. 2012, MNRAS, 420, 1926
Sobral, D., Best, P. N., Smail, I., et al. 2011, MNRAS, 411, 675
Sobral, D., Smail, I., Best, P. N., et al. 2013, MNRAS, 428, 1128
Speagle, J. S., Steinhardt, C. L., Capak, P. L., & Silverman, J. D. 2014, ApJS, 214, 15
Spinrad, H., Dey, A., Stern, D., et al. 1997, ApJ, 484, 581
Steinhardt, C. L., Speagle, J. S., Capak, P., et al. 2014, ApJL, 791, L25
Talia, M., Cimatti, A., Pozzetti, L., et al. 2015, arXiv:1508.01679
Teplitz, H. I., Collins, N. R., Gardner, J. P., Hill, R. S., & Rhodes, J. 2003, ApJ, 589, 704
Tresse, L., Ilbert, O., Zucca, E., et al. 2007, A&A, 472, 403
Tresse, L., & Maddox, S. J. 1998, ApJ, 495, 691
Tresse, L., Maddox, S. J., Le Fèvre, O., & Cuby, J.-G. 2002, MNRAS, 337, 369
Twite, J. W., Conselice, C. J., Buitrago, F., et al. 2012, MNRAS, 420, 1061
Vilella-Rojo, G., Viironen, K., López-Sanjuan, C., et al. 2015, A&A, 580, A47
Villar, V., Gallego, J., Pérez-González, P. G., et al. 2008, ApJ, 677, 169
Villar, V., Gallego, J., Pérez-González, P. G., et al. 2011, ApJ, 740, 47
Vulcani, B., Poggianti, B. M., Finn, R. A., et al. 2010, ApJL, 710, L1
Vulcani, B., Poggianti, B. M., Fritz, J., et al. 2015, ApJ, 798, 52
Whitaker, K. E., Franx, M., Leja, J., et al. 2014, ApJ, 795, 104
Whitaker, K. E., Labbé, I., van Dokkum, P. G., et al. 2011, ApJ, 735, 86
Whitaker, K. E., van Dokkum, P. G., Brammer, G., & Franx, M. 2012, ApJL, 754, L29
Wirth, G. D., Willmer, C. N. A., Amico, P., et al. 2004, AJ, 127, 3121
Wuyts, S., Förster Schreiber, N. M., van der Wel, A., et al. 2011, ApJ, 742, 96
Yan, R., Newman, J. A., Faber, S. M., et al. 2006, ApJ, 648, 281
Zhu, G., Moustakas, J., & Blanton, M. R. 2009, ApJ, 701, 86